Icarus 211 (2011) 740–757

Contents lists available at ScienceDirect

Icarus

journal homepage: www.elsevier.com/locate/icarus

Plasma, plumes and rings: Saturn system dynamics as recorded in global color patterns on its midsize icy satellites

Paul Schenk [a,*], Douglas P. Hamilton [b], Robert E. Johnson [c], William B. McKinnon [d], Chris Paranicas [e], Jürgen Schmidt [f], Mark R. Showalter [g]

[a] Lunar and Planetary Institute, 3600 Bay Area Blvd., Houston, TX 77058, USA
[b] Astronomy Department, University of Maryland, College Park, MD 20742, USA
[c] University of Virginia, Thornton Hall B102, Charlottesville, VA 22904, USA
[d] Department of Earth and Planetary Sciences and the McDonnell Center for the Space Sciences, Washington University, St. Louis, MO 63130-4899, USA
[e] Johns Hopkins University Applied Physics Laboratory, Laurel, MD 20723, USA
[f] Universität Potsdam, Institut für Physik und Astronomie, Karl-Liebknecht-Str. 24/25, D-14476 Potsdam-Golm, Germany
[g] SETI Institute, 515 North Whisman Rd., Mountain View, CA 94035, USA

ARTICLE INFO

Article history:
Received 23 February 2010
Revised 20 August 2010
Accepted 23 August 2010
Available online 25 September 2010

Keywords:
Satellites, Surfaces
Saturn, Satellites
Saturn, Rings
Enceladus
Satellites, Composition
Magnetospheres

ABSTRACT

New global maps of the five inner midsize icy saturnian satellites, Mimas, Enceladus, Tethys, Dione, and Rhea, have been constructed in three colors (UV, Green and near-IR) at resolutions of 1 km/pixel. The maps reveal prominent global patterns common to several of these satellites but also three major color features unique to specific satellites or satellite subgroups. The most common features among the group are first-order global asymmetries in color properties. This pattern, expressed on Tethys, Dione and Rhea, takes the form of a ~1.4–1.8 times enhancement in redness (expressed as IR/UV ratio) of the surface at the center of the trailing hemisphere of motion, and a similar though significantly weaker IR/UV enhancement at the center of the leading hemisphere. The peak in redness on the trailing hemisphere also corresponds to a known decrease in albedo. These double hemispheric asymmetries are attributable to plasma and E-ring grain bombardment on the trailing and leading hemispheres, respectively, for the outer three satellites Tethys, Dione and Rhea, whereas as E-ring bombardment may be focused on the trailing hemisphere of Mimas due to its orbital location interior to Enceladus. The maps also reveal three major deviations from these basic global patterns. We observe the previously known dark bluish leading hemisphere equatorial band on Tethys but have also discovered a similar band on Mimas. Similar in shape, both features match the surface patterns expected for irradiation of the surface by incident MeV electrons that drift in a direction opposite to the plasma flow. The global asymmetry on Enceladus is offset ~40° to the west compared to the other satellites. We do not consider Enceladus in detail here, but the global distribution of bluish material can be shown to match the deposition pattern predicted for plume fallback onto the surface (Kempf, S., Beckmann, U., Schmidt, S. [2010]. Icarus 206, 446–457. doi:10.1016/j.icarus.2009.09.016). E-ring deposition on Enceladus thus appears to mask or prevent the formation of the lenses and hemispheric asymmetries we see on the other satellites. Finally, we observe a chain of discrete bluish splotches along the equator of Rhea. Unlike the equatorial bands of Tethys and Mimas, these splotches form a very narrow great circle ⩽10-km wide (north-to-south) and appear to be related to surface disruption, exposing fresh, bluish ice on older crater rims. This feature is unique to Rhea and may have formed by impact onto its surface of orbiting material.

1. Introduction

Water ice on planetary surfaces is susceptible to chemical and physical alteration due to exposure to photons, charged particles, and dust. This can lead to alterations of the albedo and color of these surfaces due to, e.g., non-ice particle implantation, the formation of scattering centers, or the formation of new molecular species. Indeed, global color patterns observed on the large icy Galilean satellites have been attributed to sulfur ion implantation (e.g., Veverka et al., 1989, 1994; Grundy et al., 2007; Carlson et al., 2009), insolation, and chemical alteration by energetic ions and electrons (e.g., Paranicas et al., 2001, 2009; Khurana et al., 2007; Carlson et al., 2009).

In addition to radiation belts (e.g., Krupp et al., 2009), the Saturn system also features a diffuse ring of micron-sized particles—the

* Corresponding author.
E-mail address: schenk@lpi.usra.edu (P. Schenk).

0019-1035/$ - see front matter © 2010 Elsevier Inc. All rights reserved.
doi:10.1016/j.icarus.2010.08.016

E-ring—extending across the orbits of the inner satellite system from Mimas to Rhea and beyond (e.g., Showalter et al., 1991). Saturn also appears to experience an influx of dark material or grains (Clark et al., 2008), and possibly meteoroids or material associated with the recently discovered Phoebe ring (Verbiscer et al., 2009). Finally, Rhea itself may possess a tenuous circum-satellite ring or debris system of its own (Jones et al., 2008). Therefore, surface alterations of the icy satellites are to be expected.

Voyager and ground-based telescopes observed basic hemispheric albedo and color asymmetries on the saturnian icy satellites (Verbiscer and Veverka, 1989, 1992, 1994; Buratti et al., 1990), but these efforts did not extend into the ultraviolet (UV) or infrared (IR) and were very uneven in resolution (ranging globally from >1 km to >20 km/pixel). More recent Cassini VIMS investigations (Clark et al., 2008; Stephan et al., 2009, 2010) of several of these satellites in the visible and near-IR have confirmed these patterns and investigated potential compositional and grain-size differences.

Here we present new global, high-resolution color maps of each of the five inner midsize icy satellites, Mimas, Enceladus, Tethys, Dione and Rhea, using Cassini Imaging Science Subsystem (ISS) CCD data in three colors and at resolutions finer than 1 km/pixel. We observe the basic global color and albedo asymmetries reported earlier on most of these satellites, and we also report on significant variations from these global patterns that both reveal and constrain dynamical processes in the Saturn system. Our maps are substantially better and more uniform in resolution than was possible with Voyager data, and they extend to shorter and longer wavelengths, allowing for more definitive color mapping. Further, they allow us to compare global color patterns across the entire Saturn system interior to Titan.

2. Global mapping procedures

New 3-color maps of the five midsize saturnian satellites have been constructed from Cassini ISS Narrow Angle Camera imaging data, covering roughly 75% of their surfaces at resolutions of ~1 km/pixel (Fig. 1). Some additional areas are also covered at ~1.5 km/pixel, but no coverage was available north of +60° latitude as of this writing due to the southern declination of the Sun at Saturn when the images were acquired. These areas will be covered later in the Cassini mission. The maps are in three colors (IR3, 0.930 μm; GRN (Green), 0.568 μm; UV3, 0.338 μm, each with an effective spectral bandwidth of ~0.1–0.15 μm; Porco et al., 2004), and all images have been calibrated using CISSCAL 3.6 procedures and reference calibration files published in the Planetary Data System archives March, 2009, i.e., the most recent release available as of this writing. The maps shown here are based on global control network solutions by P. Schenk derived using ISIS2 "RAND" image control software, which allows for cartographic mapping of ISS images to precisions of a few km or better over their respective satellite surfaces. Satellite radii are from Thomas et al. (2007), with minor updates (Thomas, 2010). Mapping was completed with standard ISIS2 map projection software.

Ideally, imaging at low (i.e., <30°) phase angles (α) is preferred for color mapping as shadows are significantly reduced. However, to optimize resolution, images at a variety of intermediate phase angles ($\alpha \sim 10$–$80°$) were used as available Cassini low-phase images are often at 10 km/pixel resolution or lower. To compensate for the use of images at different phase angles, viewing angles and solar illumination, the images must be photometrically corrected to remove the effects of variable viewing and illumination and produce seamless integrated albedo maps in each wavelength.

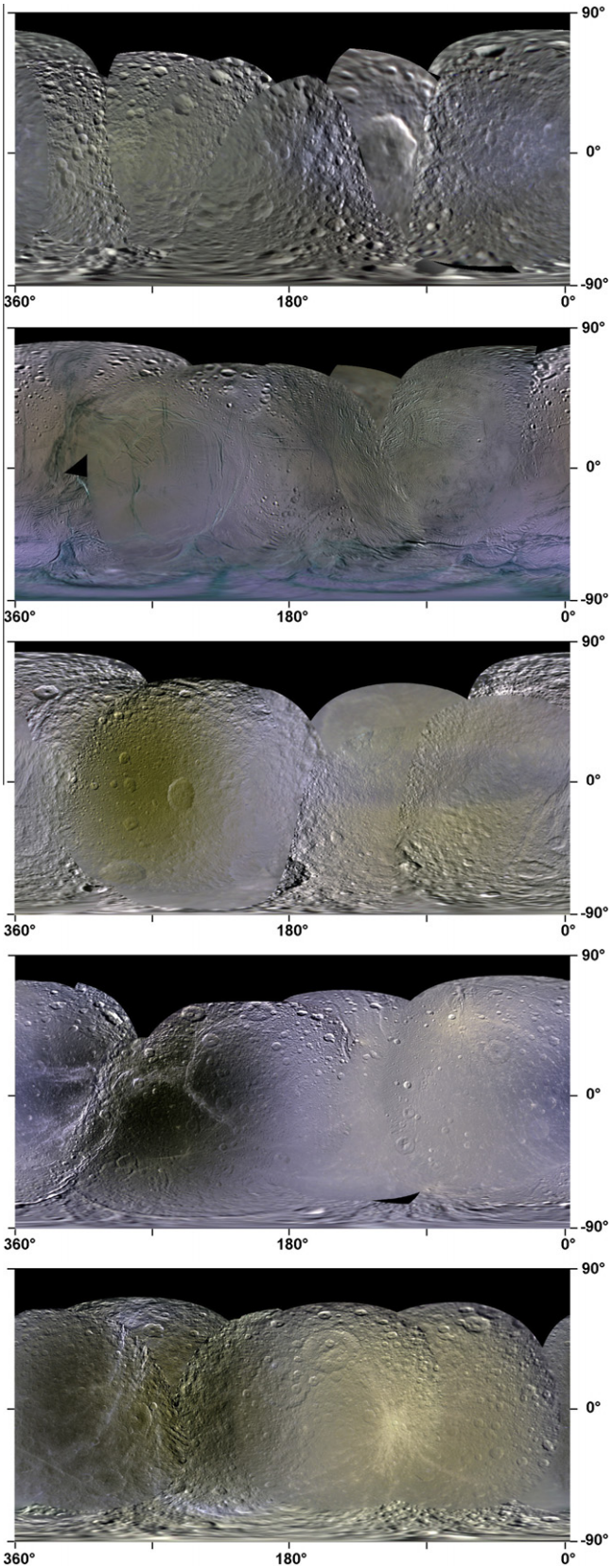

Fig. 1. Enhanced Cassini three color (IR–Green–UV filter) global maps of the five inner midsize icy satellites of Saturn (from top to bottom: Mimas, Enceladus, Tethys, Dione, Rhea). See text for detailed description. Maps are in simple cylindrical projection from 90°S to 90°N and from −2°W to 360°W.

Photometric corrections were applied using the simplified Lunar–Lambertian photometric function (cf. McEwen, 1991), which is a function of incidence and emission angles and normal albedo of the surface. The relative contribution of the lunar-like and the Lambertian components is determined by the factor $L(\alpha)$. The functional dependence of $L(\alpha)$ on phase angle varies between the satellites and sometimes between different terrains. Finally, all images are then corrected to zero phase angle (neglecting opposition surges) using a linear phase correction.

Phase functions and phase corrections have not yet been formally derived for each satellite from the relatively new Cassini data; hence preliminary values are used, derived from values used for the Galilean satellites (Schenk, 2010) and empirically adjusted for these satellites based on matching of mosaic images. Although every effort was made to produce photometrically accurate maps, it must be recognized that radiometric calibrations may be adjusted in future data releases and knowledge of photometric functions will certainly improve as data analysis continues. As a result, we focus here not on absolute albedo or color values but rather on global patterns and deviations from those patterns.

We show the maps in two forms. The first are IR–Green–UV (Fig. 1) image mosaics shown as RGB color composites, where each component also serves as an albedo map in its respective bandpass. As the filter range is beyond that of human vision, these can be considered hyper-color maps. To facilitate color pattern recognition we also show color ratio (IR/UV) maps (Fig. 2) as a direct measure of the relative spectral slope or "redness" across these surfaces. In these maps, bright features have a positive or "reddish" slope between the respective ratioed bands. Comparison with the other ratio maps shows that the IR/UV ratio provides the best color contrasts. As a rule, the G/UV maps resemble the IR/UV maps but IR/G ratio maps tend to be more bland, suggesting that many but not all of the color differences are dominated by the UV albedo.

3. Global color patterns

3.1. Hemispheric color asymmetries

Our new maps of the five midsize icy satellites of Saturn allow us to compare patterns on all five satellites and to search for variations across the entire Saturn system inward of Titan. While most show similar patterns, there are important exceptions. The outer three satellites, Tethys, Dione and Rhea, each show prominent global asymmetries in both color and albedo. The most obvious manifestation of this is the several-fold decrease in albedo across the trailing hemispheres of these three satellites (Verbiscer and Veverka, 1989; Buratti et al., 1990; Fig. 1). The color ratio maps (Fig. 2) show that this albedo decrease also coincides with a similar increase in IR/UV ratio (i.e., redness). Buratti et al. (1990) also reported a weak color asymmetry on some satellites, but the Voyager color filter range extended only from 0.4 to 0.58 μm and surface resolutions ranged from 1 to 40 km/pixel. The Cassini filters provide greater color contrast and our maps are essentially uniform and of much higher spatial resolution. For these three satellites the darkest (and reddest) materials are centered on the trailing hemisphere at the antapex of orbital motion along the equator near the 270° meridian (Fig. 2), decreasing outward radially from this point.

The magnitudes and shapes of the IR/UV peaks on the trailing hemispheres are not identical on the three satellites (Fig. 3). The IR/UV peaks on Tethys and Dione are substantially stronger than on Rhea (Fig. 3) and are best fit by Gaussian functions (Fig. 4). The IR/UV intensity increases by ~1.4 in magnitude from edge to

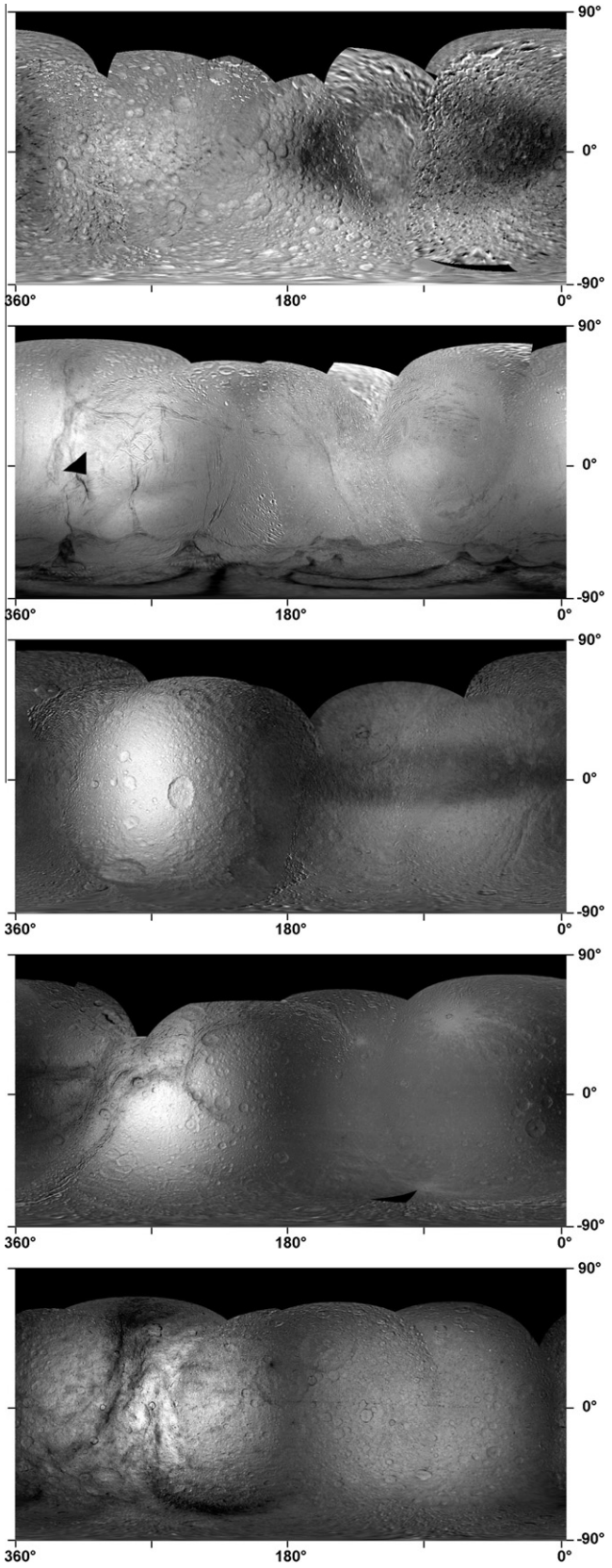

Fig. 2. Global IR/UV color ratio maps of the five inner midsize icy satellites of Saturn (from top to bottom: Mimas, Enceladus, Tethys, Dione, Rhea). Maps are in simple cylindrical projection from 90°S to 90°N and from −2°W to 360°W. See text for detailed description. Data from Fig. 1.

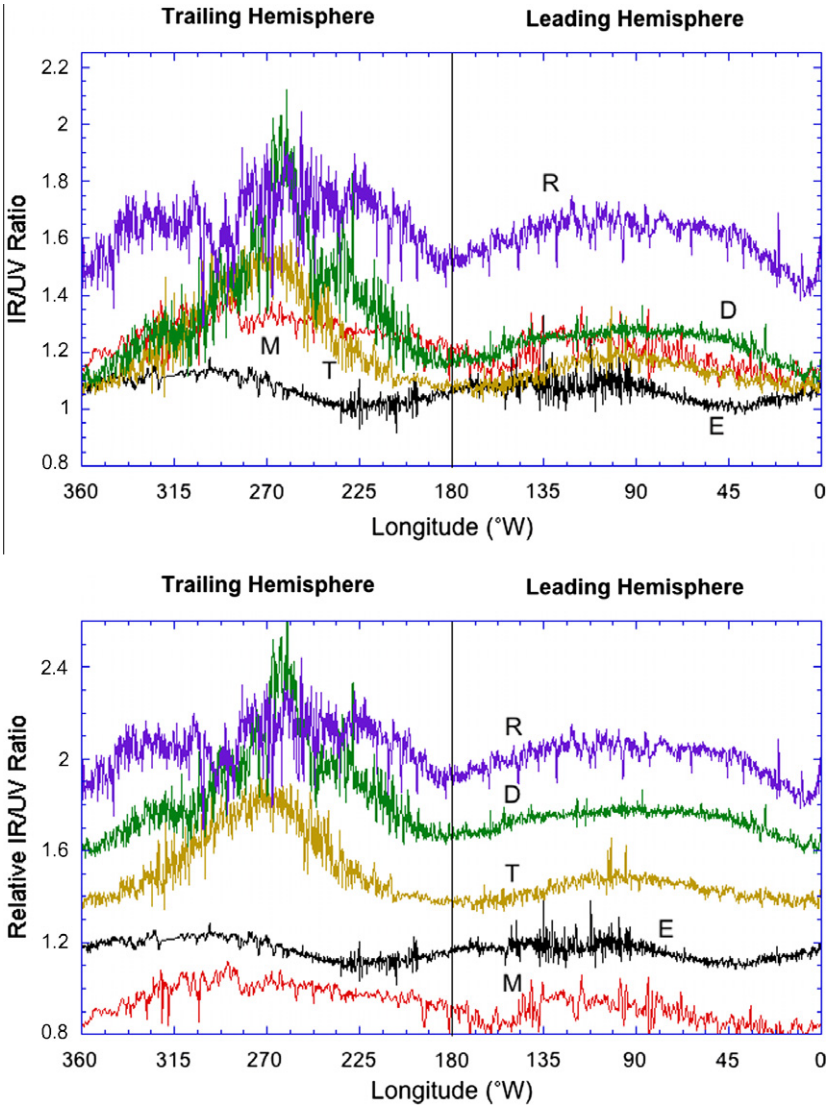

Fig. 3. East–west profiles across IR/UV ratio maps of the five inner regular Saturn satellites (M-Mimas, E-Enceladus, T-Tethys, D-Dione, R-Rhea). Traces extend along the entire equatorial circumference, beginning at 0°W longitude. In the bottom figure the profiles have been offset for greater clarity. The depressed IR/UV values in parts of the trailing hemispheres of Dione and Rhea (especially near longitude 300°) correspond to areas within and adjacent to the bright graben that cross those hemispheres (see Fig. 1). Note the offset of the pattern on Enceladus. The absolute color and photometric calibrations used here are subject to future revision and the apparent first order color differences between satellites, especially the overall redness of Rhea, may or may not be real. The jitter in the profiles provided a measure of the measurement error inherent in the data sets.

center of Tethys' trailing hemisphere, but ~1.8 in the case of Dione (Fig. 3). The center of the trailing hemisphere on Rhea is crossed by several graben or rift structures (Figs. 1 and 2), which are both bright and relatively blue[1], obscuring the center of the IR/UV peak and masking its true peak intensity and shape (similar tectonic features cross Dione but do not obscure the center of the hemisphere directly). Whether differences between the satellites relate to their relative distances from Saturn is a topic of later discussion.

A similar but weaker and previously unrecognized enhancement in the IR/UV ratio (i.e., redness) also occurs on the leading hemispheres of Tethys, Dione and Rhea (Figs. 2 and 3). Like the trailing hemisphere features, this color feature is most intense at the center of the respective leading hemisphere, but follows a smooth sine curve (Fig. 5) different in shape from trailing hemisphere features. In addition, the relative magnitude of the color feature at the center of each leading hemisphere is only ~1.1–1.2 times the intensity at the edges, considerably weaker than that observed on the trailing hemisphere *and not associated with any detectable albedo variation*. The leading hemispheres otherwise appear to be relatively bland except for this color difference. Unlike on the trailing hemispheres, the reddening on the leading hemispheres appears to be roughly consistent in shape and magnitude among the three satellites that show this feature (Fig. 5). It is therefore likely to have a different origin from the trailing hemisphere enhancements.

One curious effect of the simultaneous leading and trailing hemisphere IR/UV ratio peaks is the existence of low IR/UV (i.e., bluish) band along the boundary between the two hemispheres, forming a great-circle hoop through the poles (Figs. 2 and 3). That this band is real and not an artifact of the color mosaic process can be seen in single 3-filter observations along the boundary between the two hemispheres (e.g., Fig. 6). This bluish hoop or band may have no specific physical origin, aside from the juxtaposition of two peaked color patterns formed on opposite hemispheres, forming a natural color minimum between them.

[1] For interpretation of color in "Figs. 1, 3, 5, 6, 8, 9, 11, 13, 14", the reader is referred to the web version of this article.

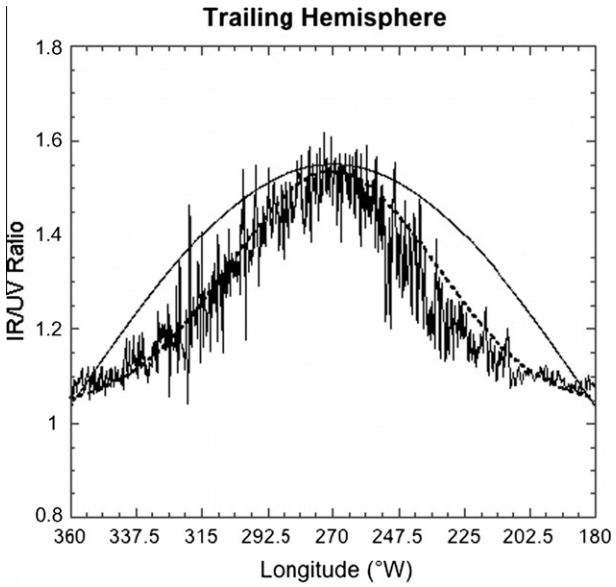

Fig. 4. Equatorial profile across IR/UV ratio map of trailing hemisphere of Tethys (from Fig. 3). A Gaussian curve (dotted line) provides a much better match to the shape of the color pattern across this hemisphere compared with that of a sine curve (solid line). A Gaussian curve also matches the Dione and Rhea patterns as well (Fig. 3), but bluish fault scarps and associated "wispy terrains" obscure large areas of the trailing hemisphere pattern on both satellites, making a curve fit difficult. Data are from Fig. 2.

3.2. Deviations from global asymmetry patterns

3.2.1. Mimas and Enceladus

Mimas does not follow the patterns described above. Mimas possesses a subtle but known leading/trailing brightness ratio in the visible that is less than unity (Verbiscer and Veverka, 1992; Buratti et al., 1998). Our maps now reveal an increase in the IR/UV ratio toward the center of the trailing hemisphere on Mimas but one much weaker than on Tethys, Dione, or Rhea (Figs. 2 and 3). The magnitude of this peak is comparable in magnitude to that seen on the leading hemispheres on those satellites, and like those patterns is not associated with the albedo decrease seen on Dione and Rhea. Mimas is heavily cratered and shadows are more prevalent on this map; additional high-resolution low-phase imaging of Mimas would provide more uniform mapping coverage and permit us to determine the physical distribution of these materials. Mimas' leading hemisphere displays an unusual pattern, though, which is not affected by phase effects, and which will be described in the next section.

Enceladus also exhibits a subtle albedo asymmetry (Buratti et al., 1990; Verbiscer and Veverka, 1994). We find in global color mapping that this active moon also exhibits a significant global color asymmetry in the form of depressed IR/UV ratios corresponding to the mapped active south polar terrains south of −50° latitude (Fig. 2), and extending northward in two progressively narrowing zones in antipodal directions up the ∼40°W and ∼220°W longitudes. The low IR/UV lobes extend to ∼55°N where color coverage is noisy or not yet available. The Enceladus color pattern differs from those described above in two important ways. First, the difference in IR/UV magnitude between the leading and trailing hemispheres, while present on Enceladus, is not nearly as pronounced as that on Rhea, Dione, or Tethys (Figs. 2 and 3). Second, the centers of enhanced IR/UV ratios are offset roughly 40° to the west of the centers of each hemisphere and hence with respect to the patterns observed on the other satellites (Figs. 2 and 3).

3.2.2. Tectonic features

As mentioned above, the only significant breaks in the trailing hemisphere color patterns on the outer three satellites, Tethys, Dione, and Rhea (Figs. 2, 3 and 7) are the linear rift/graben fractures and bright flanks (formerly collectively known as wispy terrains; Moore and Schenk, 2007; Stephan et al., 2010) on the trailing hemispheres of Dione and Rhea. These rifts and flanking deposits have markedly lower IR/UV ratios and are distinctly bluer than undisturbed terrains (Fig. 7); their relative blueness was also noted by Buratti et al. (1990). Enhanced blueness here is most likely due to relatively clean ice compared to surrounding regions (e.g., Stephan et al., 2009, 2010).

Although the global-scale color patterns on Enceladus obscure some features, there appear to be local color differences related to geologic units. The most obvious of these are the bluish "tiger

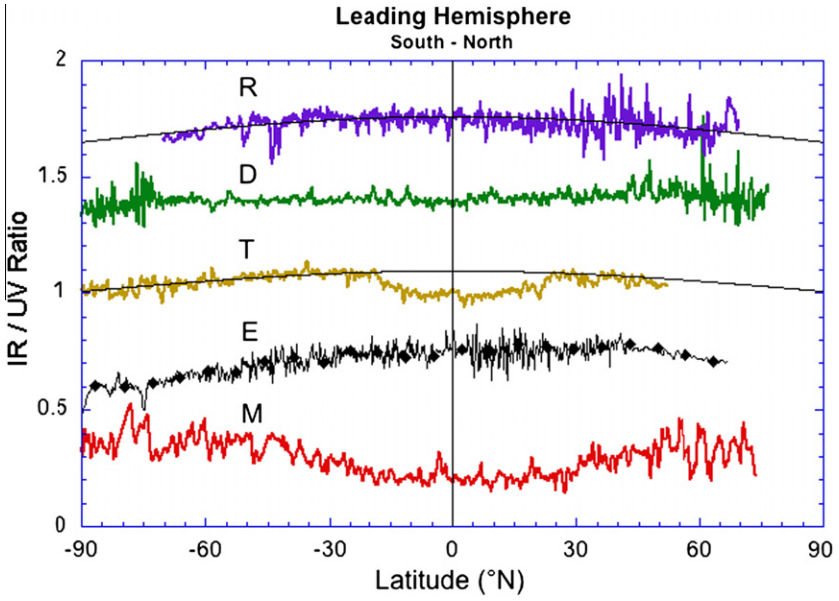

Fig. 5. North–south profiles across IR/UV ratio maps of leading hemispheres of the five inner midsize Saturn satellites. Profiles extend from pole-to-pole although north polar coverage is lacking in each case. The solid lines are sine curves. The dips in the IR/UV value along the equators of Mimas and Tethys are discussed in the text.

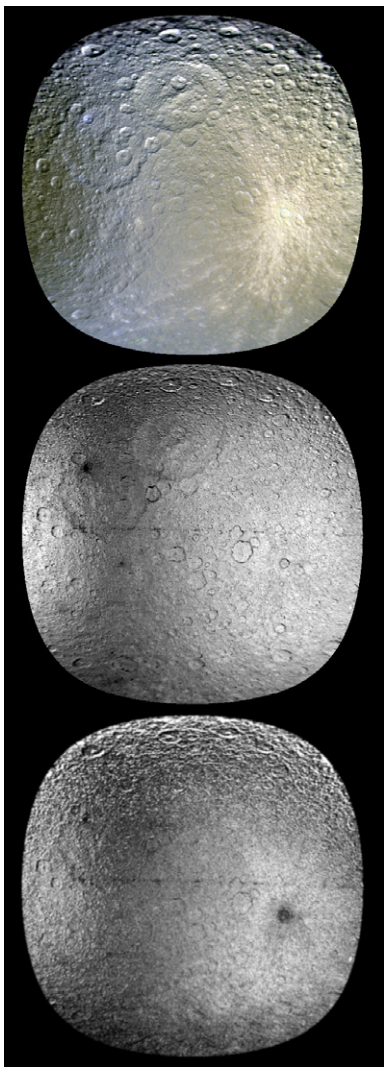

Fig. 6. Single-frame Cassini color observations of Rhea from orbit 18 along the boundary between the trailing (left) and leading (right) hemispheres. Top view is 3-color composite of IR, Green, and UV images; middle view is IR/UV ratio image (stretched to show 1.37–1.65 range); bottom view is IR/Green ratio image (stretched to 1.055–1.1 IR/UV). Views are centered near 145°W longitude, ~35° east of the boundary between leading and trailing hemisphere and clearly show the low IR/UV ratio band between the two hemispheres. The bright ray crater Inktomi at 12°S, 112°W is very prominent in the 3-color composite but is virtually invisible in the center IR/UV ratio image. The bright rays are moderately reddish (bright) while the proximal ejecta deposit is distinctly bluish (dark) in the IR/Green image. Image resolution is 1.75 km/pixel. Map extends from ~85° to 215°W.

stripes" (Porco et al., 2006) and exposed wall scarps of relatively young fault-bounded graben, including the large troughs extending northward radially from the south polar terrain boundary (Fig. 8). These cliff faces are distinctly bluish in color and may reflect the color of unaltered water ice or may reflect differences in grain size (Porco et al., 2006; Brown et al., 2006). Tectonically resurfaced regions on Enceladus are characterized by larger ice particle sizes reaching a peak near 100 μm in the tiger stripes (Brown et al., 2006; Jaumann et al., 2008); cf. the VIMS-derived 1.5-μm band depth map in Roatsch et al. (2009).

3.2.3. Impact ejecta and rim deposits

A variety of local color effects related to impact cratering can be identified. An odd color feature is the bluish (low IR/UV) colors of steep crater rim scarps in non-ancient and geologically younger craters (Fig. 7). This material may be similar to that exposed on fault scarps seen on Enceladus, at least away from the tiger stripes. Assuming that these slopes expose relatively fresh crustal material (perhaps through ongoing creep or sloughing of talus or debris downslope), these scarps may indicate that icy surfaces in the Saturn system undergo progressive reddening over time, perhaps due to mantling or alteration (such as chemical or grain size or other surface changes).

Curiously, the extremely young 48-km-wide bright ray crater at 12°S, 112°W on the leading hemisphere of Rhea (Inktomi), and likely the most recently formed large crater in the Saturn system (Wagner et al., 2007; Dones et al. 2009), is not evident in the color ratio maps (Fig. 6), except as a dark (i.e., bluish) diffuse halo surrounding the crater rim in the IR/Green ratio image. The bright rays are barely detectable in any of the ratio images. On the other hand, reddish ray patterns are clearly associated with the smaller, 31-km-wide, bright-ray central-peak crater Creusa on the leading hemisphere of Dione (49°N, 76°W; Fig. 2), despite the fact that the rays are not nearly as prominent an albedo feature as the ray crater on Rhea (Stephan et al., 2010, their Fig. 18).

We speculate we could be seeing a compositional effect. Inktomi formed on typical cratered terrain. Creusa formed on smooth plains that cover most of Dione's leading hemisphere and are interpreted to be cryovolcanic in origin (Plescia, 1983; Moore, 1984; Schenk and Moore, 2007). The Dione ray crater may have excavated through a surface deposit to redder material below. Two similar but smaller blue ray craters are also evident on this Dione terrain (Fig. 2; $D \sim 10$ km, 32°N, 134°W; $D \sim 8$ km, 64°S, 89°W).

Creusa on Dione may be the largest example of a class of "color ray craters" observed on Dione, Rhea, Tethys and Mimas (Fig. 9). These small crater rays can be either spectrally blue or red compared with background terrain. The combinations of composition and microstructure in the optical surface that are responsible for these colors are not yet clear, however. VIMS-determined water–ice band depths indicate that the bright ejecta at Inktomi on Rhea is the most ice-rich unit there (Stephan et al., 2009); similar data for Creusa on Dione imply that Creusa is likewise characterized by clean water ice, similar to the tectonic features on Dione but with the largest ice particles on Dione observed so far (Stephan et al., 2010). The predominant reddening of the Creusa rays is in contrast to the bluish coloration of exposed steep crater rims (and the general bluish color of bright rays on Ganymede [e.g., Schenk and McKinnon, 1989]), and would be difficult to explain simply as freshly exposed ice unless the colors of comminuted or melted ice excavated and deposited in rays on the saturnian satellites are affected by additional processes. Further investigation is ongoing (Schenk and Murphy, in preparation).

3.2.4. Equatorial lenses on Mimas and Tethys

An enigmatic, Voyager-era feature in the Saturn system is the dark equatorial band across the center of the leading hemisphere of Tethys (Smith et al., 1981, their Fig. 13; Stooke, 1989, 2002; Buratti et al., 1990). No satisfactory explanation has been offered for this feature, the shape of which resembles the cross-section of an optical lens. Our color maps clearly show this feature and reveal that it has a low IR/UV ratio compared to the rest of the leading hemisphere (Figs. 1 and 5), the feature being both dark in the IR and Green but bright in the UV albedo maps (see also Elder et al., 2007). Geographically, the band extends the entire width of the leading hemisphere and is symmetric with respect to the center of the leading hemisphere and the equator. It extends to approximately ±20° latitude north and south of the equator at ~90° longitude (where it is widest, spanning ~360 km), but narrows to within a few degrees of the equator at the edges of the hemisphere. We note that the center portions of the feature, nearest the equator, are not as dark or bluish as the northern and southern

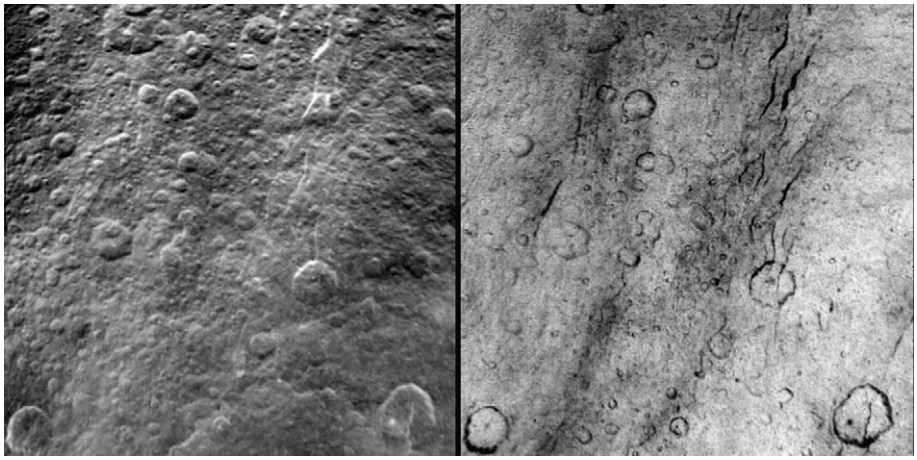

Fig. 7. Center of trailing hemisphere of Rhea, showing graben (sometimes referred to as wispy terrain) and craters. View at left is from the 1-km resolution clear-filter albedo map, at right from the IR/UV color ratio map (Fig. 2), where brightness corresponds to relative redness of the surface. Color ratio map highlights the bluish color (dark in the right view) of the graben walls and outer flanks that characterizes the wispy terrains originally seen at low resolution, and the bluish colors of rimwalls of relatively younger crater, a characteristic that fades with age. View extends from 4° to 34°N and from 266° to 304°W.

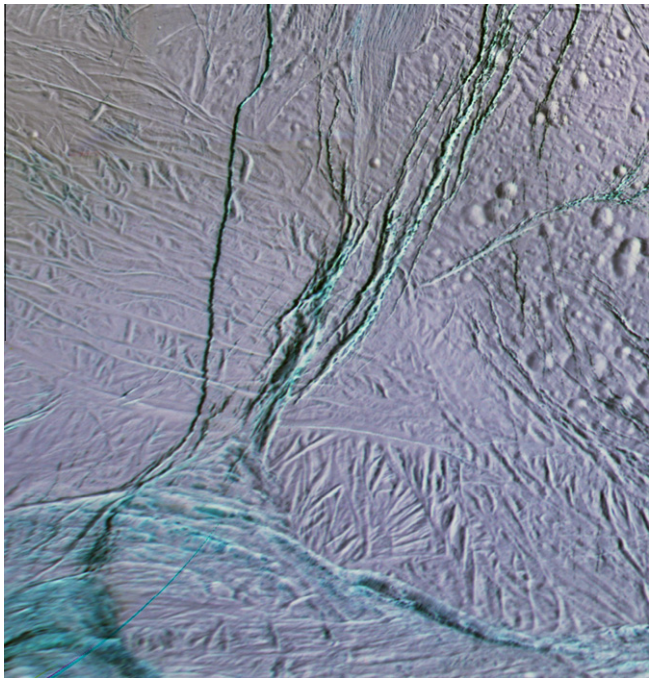

Fig. 8. High-resolution 3-color mosaic of part of Enceladus, showing bluish colors associated with relatively recently formed scarps along trough walls (center) and within the south polar terrains (bottom). Map measures ~160 km across and extends from 58 to 20°S, and 207 to 248°W.

edges, accounting for the lack of a strong signature in the profile line in Fig. 3.

One of the biggest surprises in our new color maps is the discovery of a similar lens-shaped feature across the leading hemisphere of Mimas (indeed it is the only obvious resolved large-scale color feature on that moon). This feature (Figs. 1, 2 and 5) has a similar shape to the band on Tethys, but extends to approximately ±40° latitude at its maximum extent. Due to the smaller radius of Mimas, however, this is equivalent to only ~260 km maximum width. Hence, the width of this equatorial band extends a larger spherical but shorter physical distance on Mimas. The band also wraps a few degrees onto the trailing hemisphere. The transition across the edge of this band is not sharp but gradual over a distance of roughly 25 km or so. This band also has a low IR/UV ratio, and is a bright feature in the UV albedo map, but unlike Tethys it has little or no contrast at IR or Green wavelengths (it is barely detectable as a brightening in the Green albedo map). The very low resolution and noisy Voyager color mapping coverage (Buratti et al., 1990) may explain why it was not detected in that data set.

The highest resolution color mapping of the equatorial band feature on either Mimas or Tethys is only ~1 km/pixel, insufficient to resolve whether the deposit is heterogenous at local scales or controlled by topography or surface orientation with respect to any direction. The floor of the 125-km-wide central-peak crater Herschel lies within the western half of this feature (Fig. 2) and does not appear to be as bluish as the rest of the lens. The crater floor may be less susceptible to the formation of the low IR/UV signature, perhaps due to the unusual textural properties of the floor deposits. Higher resolution color mapping of these equatorial bands should be a priority for the Cassini extended mission.

3.2.5. Equatorial great circle on Rhea

As we have seen, the color maps reveal a global color pattern on Rhea similar to that on Dione, even down to the bluish wispy streaks (originating at fractures) cutting across the trailing hemisphere. The Rhea maps also reveal numerous discrete, disconnected bluish streaks or splotches/patches. Some form an unusual, very narrow, discontinuous linear track of discrete bluish features (Figs. 1, 2, 6 and 10) along the equator of Rhea (portions of which were first reported by Jones et al. (2008a)). These particular patches are among the least red features on Rhea, and are nearly neutral in the IR–UV portion of the spectrum (Figs. 10 and 11). Once recognized in the color ratio maps, these features can sometimes be identified in the global albedo map as small spots with very slightly lower IR albedos, but otherwise have no obvious or significant albedo signature. These patches are typically no more than ~10 km wide but are often elongated along the equator forming oblong patches up to ~50 km in length. Although discontinuous, together these features form a true great circle extending from 18°E to ~275°W across the leading hemisphere and onto the trailing hemisphere (Fig. 10). This blue great circle feature is inclined very slightly to the equator (Fig. 10), tracking to ~1.8°N at ~190°W and to 1.8°S at ~20°W. Detailed mapping in the ~75°W longitude section suggests that the great circle trace may have a bend or kink along it (Fig. 12).

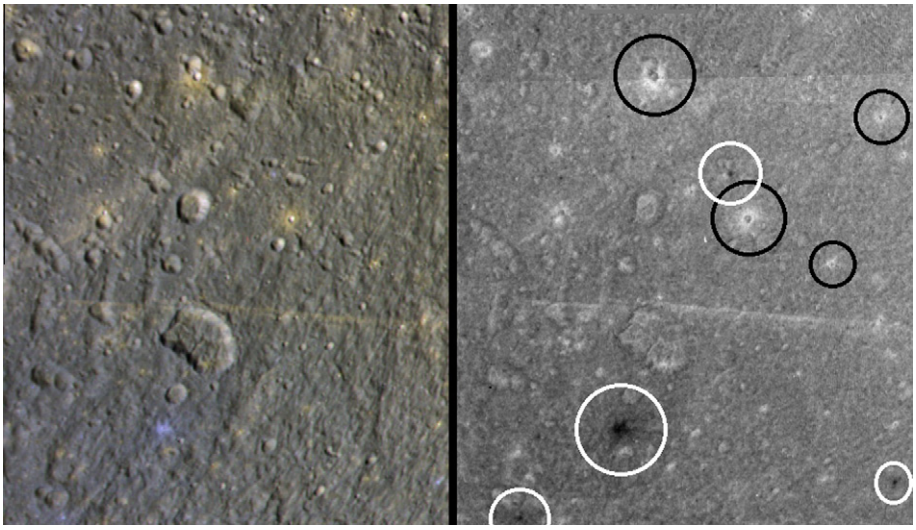

Fig. 9. Enlargement of 3-color mosaic (left) and corresponding IR/UV ratio map (right) of Dione. Highlighted are several red- and blue-rayed impact craters. Scene is ~200-km across, centered on 25°S, 142°W.

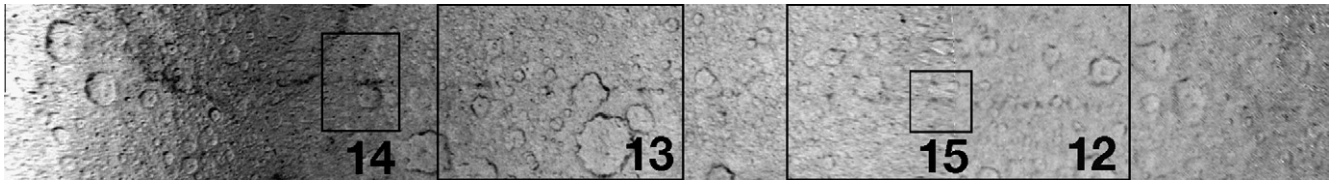

Fig. 10. Enlargement of leading hemisphere of global IR/UV color ratio image of Rhea. Region is centered on equator and extends from 358°W to ~195°W. Black boxes show locations of enlargements shown in Figs. 12–15.

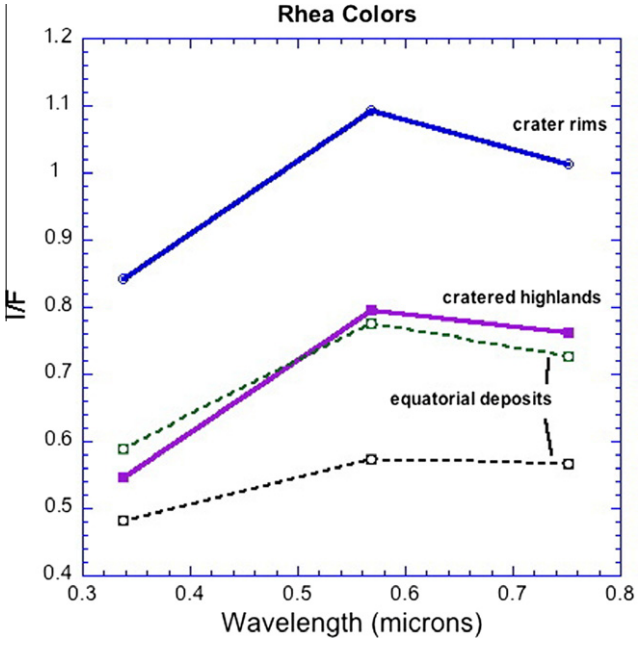

Fig. 11. Color values of select geologic units on Rhea. Bluish equatorial patches are shown as dashed lines. Data values are from 5 × 5 to 9 × 9 pixel samples of the images with standard deviations of ~0.02 (I/F). Based on 260 m resolution images acquired in the IR1, Green and UV3 filters and shown in Fig. 14. Ring deposits in blue splotch shown in Fig. 13 are among the least reddish units on the surface.

Fig. 12. IR/UV ratio image of equatorial patches on Rhea. Single-frame 3-color observation (i.e., no mosaic seams) is from Cassini orbit 5 and extends from 50° to 100°W (or 700 km) and from 20°S to 20°N. Thin line traces line of constant latitude (−1.3°). Blue patches east of 73° longitude lie along this line, those to the west lie to the north, indicating a minor kink or deviation in the distribution of patches.

The character of the patches appears to change on the trailing hemisphere, where they are characterized by lower albedo and colors indistinguishable from the general reddish tones of that hemisphere. There appears to be a gap in the great circle between ~275° and ~340°W, but this also the region where the wispy terrains are most intensely developed (potentially masking these colored patches) and where color imaging has the lowest spatial resolution on our map. Given that color observations of Rhea's

trailing hemisphere are not yet as high in spatial resolution as those on the leading hemisphere, our characterization of the spots there may change when these data become available. Altogether though, these discrete, narrow, bluish patches are distinct from the much broader and diffuse equatorial lenses of Mimas and Tethys. No evidence has been found for similar discrete equatorial features on any of the other midsize icy saturnian satellites.

On Rhea, several blue patches between 110° and 155°W longitude were observed at 0.53 km/pixel in three colors and in stereo, providing concurrent DEM coverage (Fig. 13). The highest resolution (0.28 km/pixel) stereo color observation of a blue patch was acquired along the equator between 161° and 165°W (Fig. 14), together with one concurrent 140 m/pixel clear filter mapping image. The 161–165° observations are in the same filters as the global maps, except that here the IR1 filter, at 0.742 μm, was used. Even at this higher resolution, there is only a slight albedo signature of these color features; they are distinguished mostly by color.

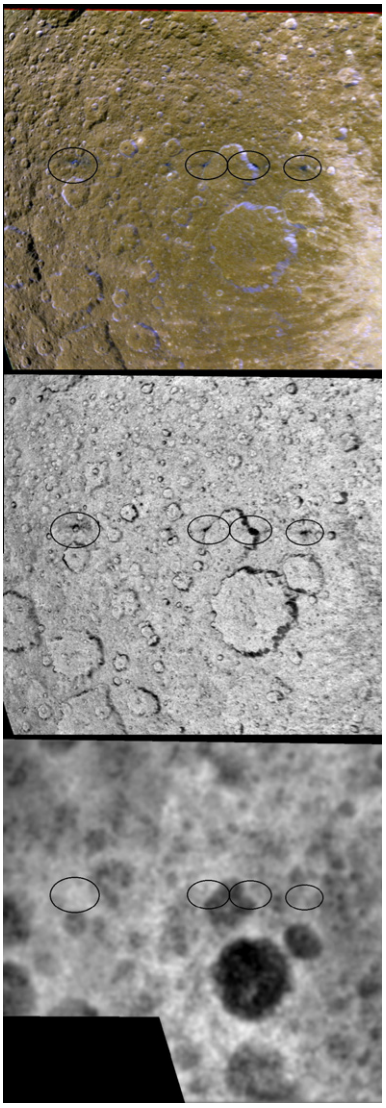

Fig. 13. Medium-resolution observations along the equator of Rhea. (top) Three-color mosaic from IR, Green, and UV channels (see text); (center) IR/UV ratio image; (bottom) Digital elevation model (shown in gray-scale with dynamic range of 7 km). Views centered on 0°N, 130°W at resolution of 530 m/pixel. Oval circles highlight locations of prominent equatorial spots described in text. Note bright rays from Inktomi, the bright ray crater at 12°S, 112°W extending into the eastern edge of the mosaic. The bluish rim scarps (dark in the IR/UV map at center) are also apparent. View extends from 117° to 155°W longitude.

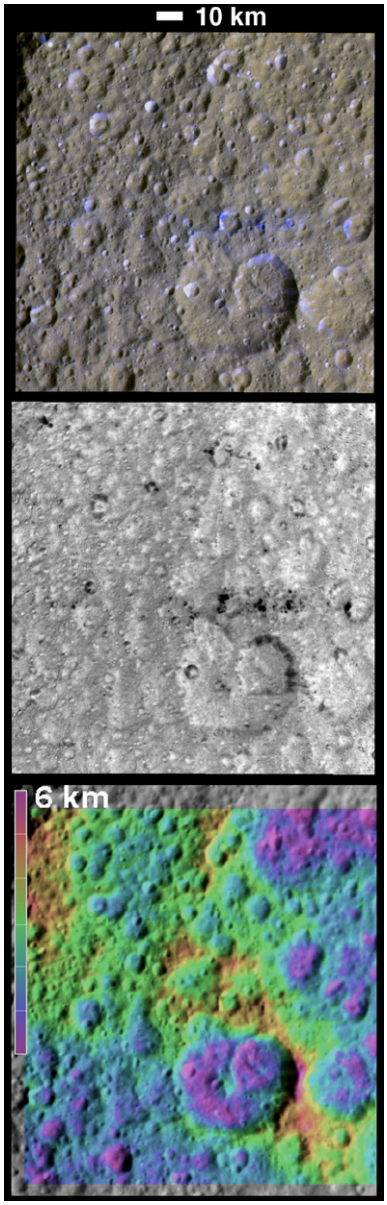

Fig. 14. High resolution (140 m/pixel) *Cassini* observations along the equator of Rhea. View centered on 0°N, 163°W. (top) Three-color mosaic (in IR1, Green, and UV3 filters); (center) IR1/UV color ratio image; (bottom) Color-coded stereo-derived DEM combined with image mosaic. Topography shown has a total vertical range of 6 km.

Both observations show that the blue patches are not associated with any tectonic features such as graben, fractures or ridges.

The 161–165°W patch (seen in the global map as an elongate feature) is resolved at higher resolution into a number of discrete bluish deposits mostly associated with impact craters ~0.5–11 km across (Fig. 14). In smaller craters the bluish materials are confined to crater rims and sometimes crater floors; in larger craters, only the rim scarp is distinctly colored, and most prominently on the western (east-facing) rimwall (although there may be shadowing effects on eastern rimwalls). Mapping at 850-m resolution in the 80°W longitude region also demonstrates that the most prominent exposures of bluish material appear to be on east-facing slopes (Fig. 15). These rim scarp materials are similar to but even more bluish than material exposed on rimwall scarps of relatively young craters observed globally (Fig. 7). Irregular unresolved bluish patches 1–5 km across also occur within the general area of

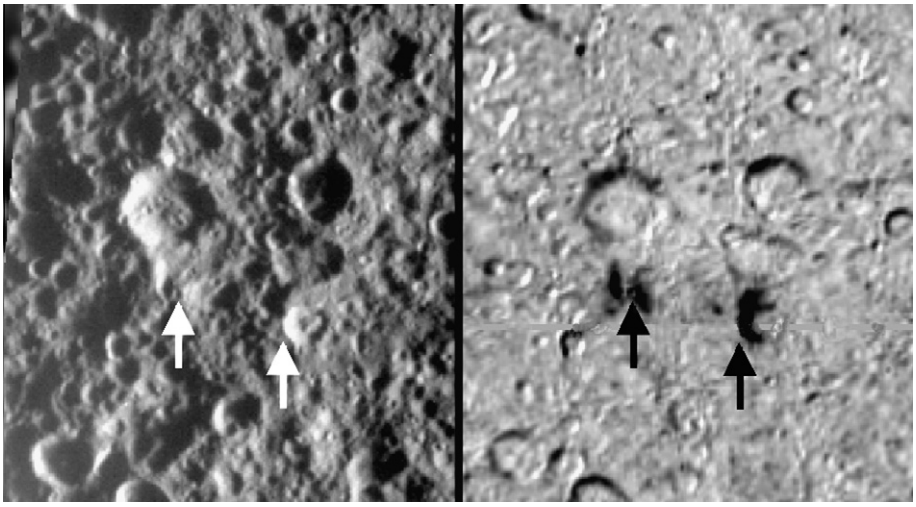

Fig. 15. Image mosaic (left) and IR/UV ratio image of region centered on 0°N, 79°W on Rhea. Image was acquired early morning local time and highlights topographic relief. Arrows point to local landmarks in both maps, indicating that the bluish equatorial material in this region occurs dominantly on east-facing slopes. Area shown is 110 km across.

the 161–165°W blue patch. These do not appear to be associated with resolvable impact craters. Not all craters within the confines of the low-resolution blue patch are spectrally distinct, however; some of the small craters appear spectrally "normal" and have no unusual coloration.

The two resolved sites with topography reveal that the blue patches lie on high-standing topography. At ~125°W, blue patches lie atop the steepest and highest parts of the rim of an irregularly shaped, 55-km-wide impact crater (Fig. 13). The 161–165°W blue patches lies across the top of an irregularly shaped, north–south trending ridge (Fig. 14), roughly 3 km high relative to the local mean topography. The ridge is part of Rhea's general global pattern of rugged cratered topography and is not unique, but the blue streak deposits are most prominently developed on the east-facing slopes of this irregular ridge. These observations indicate that blue material deposition was controlled by regional and local topography, favoring local high-standing topography and steeper slopes, possibly east-facing slopes (e.g., Fig. 15).

3.3. Summary of color patterns

In this section we summarize the complex overlapping color patterns we have identified on the inner five icy midsize saturnian satellites. There are at least five distinct color features that have been identified. In this context, "bluish" describes the spectral slope in the IR/UV region relative to colors of adjacent or globally distributed features.

1. *Trailing hemisphere reddening.* The outer three of the midsize satellites under consideration, Tethys, Dione and Rhea, are characterized by a significant reddening increasing towards the center of the trailing hemispheres, where the relative IR/UV ratios are enhanced by factors of 1.4–1.8 over those measured along the edges of these hemispheres (Figs. 1–3). This reddening is also associated with a general darkening towards the centers of the trailing hemispheres. No pattern of this type is seen on the trailing hemisphere of Mimas.

2. *Leading hemisphere reddening.* The outer three satellites, Tethys, Dione and Rhea, are also characterized by a significant (though lesser) reddening of their leading hemispheres (Figs. 1 and 2). IR/UV reddening ratios near the center of these hemispheres are 1.1–1.2 times higher than those along the edge of the hemispheres. Unlike the trailing hemisphere pattern, this color variation not associated with a darkening but rather a general uniformly bright albedo. A similar pattern may occur on the *trailing* hemisphere of Mimas, but color data are relatively lower in spatial resolution and are noisy on this satellite.

3. *Equatorial bands.* Broad bands of bluish (low IR/UV ratio) material extend across the leading hemispheres of both Mimas and Tethys (Figs. 1 and 2). The band extends ~40° north and south of the equator on Mimas, and ~20° on Tethys. Each band extends only a few degrees onto the trailing hemisphere of each satellite. The band is superposed on the leading hemisphere reddening on Tethys. No similar bands have yet been identified on other satellites.

4. *Rhea equatorial great circle.* Unique to Rhea is a sequence of bluish (low IR/UV) patches aligned in a great circle oriented ~1.8° to the equator (based on our current best mapping coordinates; Figs. 10 and 12). The bluish material is at most 20 or so km wide (north-to-south) and extends in discrete discontinuous patches across the entire leading hemisphere and in more widely separated patches across portions of the trailing hemisphere (where currently available color imaging is of lower quality). Unlike the other global scale features, these are discrete spots most often associated with particular impact craters or crater rims located along the equator.

5. *Enceladus.* The color patterns on Enceladus are distinct from the other satellites (Figs. 1 and 2). A reddening occurs on both leading and trailing hemispheres, but unlike the outer three satellites, they are offset 40° or so to the west of the centers of these hemispheres. No darkening of the trailing hemisphere is observed. Two asymmetric zones of bluish material extend north by northeast from the edge of the south polar tectonic terrains (which are themselves bluish).

6. *Geologic features.* Recently exposed or young surfaces on these satellites tend to be relatively less red in color (and may be essentially neutral in the mapped spectral range). These include younger fault scarps on Enceladus and rim scarps of relatively young craters on Rhea, Tethys and other satellites (Figs. 7 and 8). Additional geologic features include crater ejecta rays with relatively bluish or reddish color. Detailed mapping of color properties of geologic units will be addressed separately from this report.

4. Origins

Our new Cassini 3-color maps of the five inner midsize icy satellites of Saturn reveal basic global asymmetries as well as several

major deviations from these patterns. This suggests that processes inherent to the dynamics of the Saturn system are involved, but that in some cases, satellite-specific processes can also be involved in altering the surfaces of these icy moons. We will discuss each of these aspects in turn.

4.1. Global asymmetries – role of the E-ring

Across the orbital space spanned by Mimas to Rhea, satellite albedo anti-correlates with distance from Enceladus, and indeed to the surface density of the E-ring (e.g., Pang et al., 1984; Verbiscer et al., 2007). Verbiscer et al. (2007) in particular argue that the anomalously large opposition surges and large geometric albedos (in the visible) of all five midsized satellites are due to E-ring particles, now known to be resupplied by Enceladus' plumes, "sand-blasting" (their term) satellite surfaces and the resulting ejecta recoating the surfaces with icy microstructures, although the details are far from understood.

The basic leading–trailing albedo asymmetry of the outer three moons considered here (Tethys, Dione, and Rhea) has been known since before Voyager days (cf. Buratti et al., 1990), and may also be due to interactions with E-ring particles. Horanyi et al. (1992) and Hamilton and Burns (1994) analyzed the orbital motions of ~1-μm particles leaving Enceladus and found that they would evolve considerable eccentricities. At apoapse, such particles would be moving more slowly than circular orbital speeds, and thus would be preferentially swept up by the leading faces of satellites such as Tethys, Dione, and Rhea. Hamilton and Burns (1994) offered that this was the root cause of the leading-hemisphere brightening seen on these three worlds. Conversely, the trailing hemisphere of Mimas should be brightened by E-ring particles at periapse overtaking that satellite. Mimas' trailing hemisphere is indeed the brighter of the two (Verbiscer and Veverka, 1992; Buratti et al., 1998), as is Enceladus' (Verbiscer and Veverka, 1994; more on this below).

There are of course a number of potential physical effects or mechanisms that may contribute to leading/trailing hemispherical albedo, color, or other asymmetries. Smith et al. (1981) offered that enhanced bombardment by heliocentric impactors (so-called population III) on the leading hemispheres of tidally locked satellites could be responsible for eroding, erasing or suppressing endogenic or otherwise older, intrinsic albedo patterns. Conversely, Clark et al. (2008), based on a careful analysis of VIMS spectra across the surface of Dione, reject this hypothesis. Rather, they argue that the lower albedo on the trailing hemisphere is due to implantation of fine (sub-micron) dark particles, particles so fine they cause a Rayleigh-scattering reflectance peak in the visible, and in addition, are absorbing in the UV–visible shortward of ~0.5 mm. Additional spectral evidence is presented in Clark et al. (2008) and Jaumann et al. (2009) that this dark material is widespread in the saturnian system, and may be primarily composed of finely divided (nanophase) iron and/or iron oxide (e.g., haematite) particles (cf. Kempf et al., 2005). Noll et al. (1997) offer that the UV absorber is carbonaceous. Whether this dark material is cometary in origin, related to the Phoebe ring (Verbiscer et al., 2009), or something else entirely, is not known at this time.

In Saturn orbit, particles smaller than about 0.05 μm in radius are electromagnetically dominated and behave roughly like ions corotating with Saturn's magnetic field, and overtake the satellites from behind (Hamilton 1993; Dikarev 1999). Dust grains 0.2 and 0.5 μm in radius, although gravitationally dominated, orbit Saturn 10% and 1.5% faster than the Keplerian rate, respectively (Hamilton, 1993). *If* grain orbits are nearly circular, these grains will also overtake the satellites from behind, and thus be consistent with the hypothesis of Clark et al. (2008). However, it is known that the equilibrium potential of larger (e.g., E-ring) grains changes sign at a radial distance close to Rhea's orbit (Kempf et al., 2006). Thus, super-Keplerian orbital speeds should obtain for such larger grains at Tethys, Dione, Enceladus, and Mimas, where the potential—and grain charge—is negative, but this may not necessarily be true at Rhea, where the potential is close to zero, and might even assume positive values. That is, grains larger than ~0.2 μm, if moving on circular orbits, may move at near- or sub-Keplerian speeds there (Kempf et al., 2006).

Thus, based on the above, there would appear to be at least 3 classes of particles whose bombardment could contribute to the hemispheric albedo and color patterns seen on the inner midsize icy satellites: E-ring particles, small heliocentric impactors, and sub-micron dark particles. There is naturally also the direct effect of magnetospheric plasma bombardment, which to first order concentrates on the trailing hemispheres (and is discussed in greater detail below). Bombardment of charged particles can implant new chemical species, can drive chemical reactions and species creation, alter grain size and other microstructure (thus affecting absorption band depths), and even sputter away the surface. At Europa, for example, the trailing hemisphere is darkened and reddened by the implantation of sulfur into the surface ices (e.g., Johnson et al., 2004). In the Saturn system, the inner magnetospheric plasma is dominated by water and water products and sulfur is unknown. Indeed, S is very under-abundant in the plume gas emanating from Enceladus, whereas CH_4 and other organic compounds are present at the percent level (Waite et al., 2009), so perhaps carbon is the active implanted species in terms of albedo and spectral slope variation.

Now, it is not clear whether bombardment of essentially clean, water–ice surfaces by such relatively "innocuous" species as OH^- and O^{++} (at Saturn) should produce pronounced albedo or color changes. Certainly, the production of interstitial H_2O_2 or O_3 ought not by itself lead to dramatic changes in ISS colors (although the UV filter set is sensitive to the 0.26 μm ozone absorption band and the onset of absorption by H_2O_2 at 0.3 μm; cf. Noll et al., 1997; Carlson et al., 1999; Fig. 20 in Porco et al., 2004). Microstructural changes (discussed below) are another matter. Yet another possibility is that preferential sputtering of water ice from the trailing hemispheres may enhance the abundance of any more refractory (possibly iron-rich), dark particles there.

In sum, E-ring particles (mainly water ice), heliocentric impacts, sub-micron dark particles, and magnetospheric plasma may all contribute to the leading/trailing albedo and color asymmetries, whether pronounced or subtle, on Mimas, Enceladus, Tethys, Dione, and Rhea. To the extent our Cassini-ISS-derived albedo and color maps (Figs. 1 and 2) corroborate previous ground-based and Voyager results, previous conclusions are supported. In particular, an important role for E-ring particle bombardment is necessitated by the global geometric albedos of all five satellites (Verbiscer et al., 2007) and by the near-equal reflectances, if not brighter trailing hemispheres, of Mimas and Enceladus (Buratti et al., 1998). Indeed, without Enceladus' unique (plume and E-ring) contributions, it would be very difficult to explain why Mimas and Enceladus do not mimic Tethys, Dione, and Rhea in terms of hemispheric albedo and color.

In contrast, Stephan et al. (2010), in their very detailed VIMS-based study, were not able to find compositional or grain-size evidence of a preferential leading hemisphere bombardment by E-ring particles on Dione. It is not clear, however, what one should expect in this regard from a bombardment by microscopic water–ice particles of a water–ice surface. Our maps (Figs. 1, 3 and 6) do provide an interesting piece of the puzzle, the "blue valleys" between the leading and trailing hemispheres (0° and 180° meridians) of Tethys, Dione, and Rhea. In other words, the brighter, leading hemispheres do not continue to get bluer as the apex of motion is approached. Rather, they become slightly more red

(Figs. 3 and 5). This behavior is not obviously captured by any of the mechanisms described above.

A simple explanation for the reddish color peaks at both the apex and antapex of motion on these moons is that one or more of the unidirectional solid or charged particle bombardment mechanisms is operating, but that the apex and antapex of motion have exchanged positions due to a suitably large impact (Chapman and McKinnon, 1986). We regard this as highly unlikely, however, as all four moons (Mimas, Tethys, Dione, and Rhea) would have had to have undergone such a reorientation; moreover, any such impact would have likely completely reset the moon's optical surface.

A more intriguing, albeit speculative, idea is that Saturn's magnetic dipole reverses on a suitable time scale. The orientation of the magnetic field would not of course affect the motion of the thermal plasma, or that of particles so small as to be swept along with the corotating field. They would still bombard the trailing hemispheres of motion. Nor would the gravitational focusing of heliocentric bombardment onto the leading faces be affected. But the Lorentz force that larger orbiting particles would feel would be reversed. In particular, E-ring or dark particles in the ~0.1–1 mm range would have their *circular* orbital speeds switch from super-Keplerian to sub-Keplerian. These particles would then be subject to sweep-up by the leading hemispheres of the satellites. In this scenario, the subtle reddening as the apex of motion is approached is a relict of an earlier time, and is slowly disappearing under the combined influence of present-day heliocentric micrometeorite and/or eccentric E-ring particle bombardment.

4.2. Charged-particle radiation effects

Because the inner midsize icy satellites orbit within Saturn's magnetosphere, the trapped particle radiation there "space weathers" the surface materials, as at the Galilean satellites (Johnson et al., 2004; Carlson et al., 2009). Due to the large number of neutral atoms (and grains) in the inner magnetosphere of Saturn, the plasma/particle situation there is unique. Cold, corotating, plasma ions survive the effects of the neutral gas, because in collisions a cold ion is simply replaced by another cold ion (i.e., there is no net loss of an ion). At higher energies, however, ions undergo charge-exchange whereby an energetic ion becomes an energetic neutral and exits the system, leaving behind a cold ion (e.g., Paranicas et al., 2008). Therefore, the regime close to Saturn in which these satellites reside is unlike that at Jupiter, where the population of ions between the plasma energies (eV) and the energetic ions (tens to hundreds of keV) is quite "robust" (i.e., the ion energy distribution is broad, e.g., Mauk et al., 2004).

For electrons, it is the particles in the MeV or so energy range that form Saturn's *radiation belts* (e.g., Paranicas et al., 2010a). The radial extent of the belts varies by energy, but these particles are most important out to about the orbit of Tethys. Furthermore, these particles drift in retrograde around the planet and initially impact the leading hemispheres of the satellites (see below). However, in the tens to hundreds of keV energy range, the electrons are at their highest fluxes near Dione and Rhea (e.g., Carbary et al., 2009). Inward of these satellites, electrons in the tens to few hundreds of keV fall off rapidly in intensity (Paranicas et al., 2010b, in preparation). In any event, these lower energy electrons preferentially impact the trailing hemispheres of the satellites.

Charged-particle radiation can produce a variety of effects, including reddening and brightening, depending on the wavelengths in question as well as the composition and energies of the incident particles. Although carbon ions are present in the saturnian plasma as trace species, as noted above no single dominant ion, such as sulfur from Io in the jovian system, is known to readily affect satellite surfaces by implantation. Energetic ions and electrons on the other hand can also affect surfaces by causing chemical and physical alterations. For energetic ions and electrons it is their energy (which dictates which hemisphere they will preferentially impact) and energy spectrum at each body that is important.

That radiation processing *is* occurring on the midsize icy satellites is clear from the detection of an ozone absorption feature, at 0.26 μm, in the surface ice on Dione and Rhea (Noll et al., 1997). Reddening may also occur *in the UV* due to formation of carbon residue associated with radiation-processed, implanted carbonaceous material (Noll et al., 1997), although Clark et al. (2008), Stephan et al. (2010), and Jaumann et al. (2009) argue that carbon particles are themselves insufficient to explain the total UV absorption seen by VIMS at Dione and elsewhere. Regardless, that radiation processing in an ice matrix should result in *some* radiation darkening at wavelengths relevant to the Cassini ISS UV filter set (specifically, the UV1 and UV2 filters) is not unreasonable (e.g., Noll et al., 1997; Carlson et al., 2009; Hendrix and Johnson, 2009). We note that the ambient, thermal plasma in this region of Saturn's magnetosphere, though non-negligible (Johnson et al., 2008), has much lower energies and, hence, smaller penetration depths than the plasma at Europa. Therefore, the higher-energy ions and electrons that are energized outside of Rhea's orbit and diffuse inward are likely the dominant agents for radiation effects.

As noted above, inwardly diffusing tens to hundreds of keV electrons primarily affect Dione and Rhea (for ions, Rhea principally [Paranicas et al., 2008]), likely producing the observed ozone-like features. These two satellites are probably more heavily weathered by these charged particles, which have energies below the radiation belt energies, than are Mimas, Enceladus, and Tethys. In contrast, the net irradiation effect of the thermal plasma is minor. Such electrons and ions bombard in an axially symmetric pattern with its peak on the trailing hemisphere, the principal effect likely being modestly enhanced absorption in the UV on the trailing hemispheres (by any or all of the mechanisms just discussed).

That the asymmetric color patterns on both the leading and trailing hemispheres are directional in nature and not isotropic is suggested by the distribution of color patterns within craters near the edges of these hemispheres. Comparison of color patterns within craters near the leading–trailing hemisphere boundary on the anti-saturnian side of Dione show that crater walls facing toward the apex (if on the leading hemisphere) or the antapex (if on the trailing hemisphere) are often distinctly redder than walls facing the opposite directions (Fig. 16). Crater walls typically slope between 20° and 40°. Thus crater rims nearer the edge of each hemisphere are going to be more effectively shielded if they face away from the direction of incoming debris or thermal plasma, whereas slopes facing toward those directions are more likely to accumulate those deposits or effects. In the case of the leading hemisphere, E-ring debris will accumulate more efficiently on rimwall slopes facing toward the apex (as shown in Fig. 16). On the trailing hemisphere, plasma bombardment will alter surface colors more efficiently on rimwalls facing the direction of incoming plasma (the antapex). This process apparently operates in competition with formation and/or preservation of bluish rimwall scarps, leading to complex color patterns at high resolution in some regions on these satellites, especially near the boundaries between the two hemispheres (e.g., Fig. 16).

4.3. Equatorial bands of Mimas and Tethys

The fact that equatorial lenses form on both Mimas and Tethys suggests that a system-wide process not restricted to one satellite is operative. A similar lens-shaped albedo/color pattern is evident on Europa (Fig. 1 in Paranicas et al. (2001)), but the more complex geologic patterns of Europa makes the feature there less obvious. The latter pattern is attributed to bombardment by very energetic

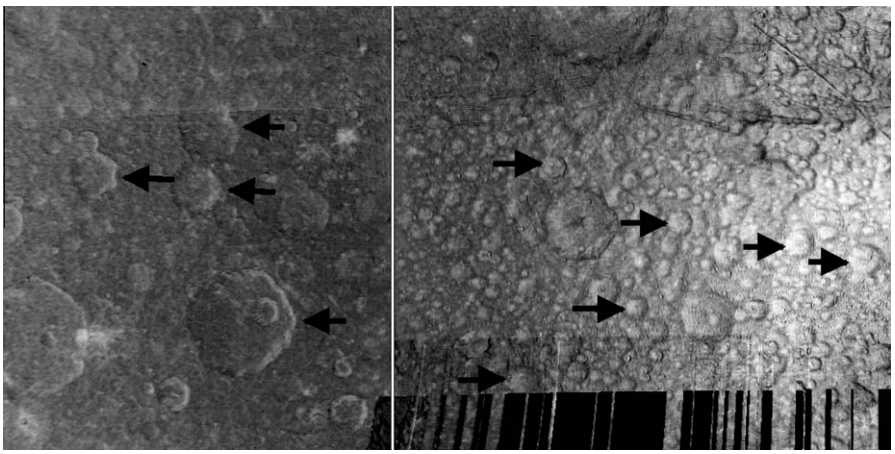

Fig. 16. IR/UV ratio map showing colors along the boundary between leading (right) and trailing (left) hemispheres of Dione. Arrows indicate sides of craters with "reddish" spectral properties. These crater walls face the centers of their respective hemispheres. Vertical white line is 180° longitude. Black hash marks are missing data. Map resolution is 1 km/pixel.

electrons onto Europa (Paranicas et al., 2001). These particles preferentially impact the trailing hemisphere of that moon at equatorial latitudes. The electron energy dose into the surface also dominates the total dose from energetic charged particles. Whereas Europa is deep in the electron radiation belt of Jupiter, Mimas, Enceladus and Tethys are all in the electron radiation belts of Saturn. Curiously the oval albedo/color pattern occurs on the hemispheres opposite to that of Europa (though not at all on Enceladus due to the dominance of local resurfacing there).

Here we propose that the different placements of the lens-shaped bands at Europa and Mimas/Tethys are related to the net motion of radiation belt electrons at Jupiter versus Saturn. Whereas most charged particles circle Saturn in a prograde manner, like the satellites, very energetic electrons (>1 MeV) can have a net drift in the opposite direction. At Europa's orbit, the equivalent energy transition occurs at approximately 25 MeV, meaning that only electrons above this energy preferentially impact the leading hemisphere of Europa, but these electrons do not contribute much to the total radiation dose (Paranicas et al., 2009). At Mimas and Tethys, the strengths of the planetary magnetic field are such that this transition energy is much lower. Electrons above a certain energy have net guiding center motion that is opposite to the motion of the inner satellites. For Mimas (Tethys), the range of energies above which electrons impact the leading hemispheres of the satellites is 1.0–1.25 MeV (0.9–1.1 MeV). These ranges cover equatorial pitch angles between about 30° and 90°. Roussos et al. (2007, their Fig. 1) show these values for several inner satellites.

To quantify this proposal, we have calculated the dose into the leading hemispheres of Mimas and Tethys associated with these energetic electrons. Inside the orbit of Dione, electrons with energies above about 1 MeV preferentially bombard the leading hemispheres, and this is also the region in which the intensity of the MeV electrons becomes a substantial component of the energetic plasma.

For energetic electrons above the transition energy (i.e., those that are colliding preferentially with the leading hemispheres of the inner saturnian satellites), the spread of the bombardment in satellite latitude depends on the energy. For example, at higher energies, electron guiding centers have greater relative speeds to the satellites. The basic physics governing the interaction is the speed of the electrons along the magnetic field line compared to their flow (drift speed) perpendicular to the field lines. When the drift speed increases, the electrons reach higher latitudes on the surface. For instance, in the rest frame of the satellite, electrons that are moving onto the leading hemisphere of Tethys at low speed will all be lost close to the equator of that moon. Electrons moving at high speed will reach higher latitudes on the moon before being completely lost. For a 1 MeV electron near Mimas' (Tethys') orbit, the gyroradius of a particle mirroring at ±34° latitude is 3.2 km (12.7 km). Thus, because these values are small compared with Moon radii, we do not explicitly include the effects of gyroradius in generating the bombardment patterns.

To quantify this we have calculated the energy flux into the surface. For an isotropic flux, this flux can be estimated from the following integral over particle energy E,

$$P = \pi \int j(E) E\, dE \tag{1}$$

In the calculations here, we instead consider a simple trapping distribution at all energies and perform the integral from the energy of net retrograde motion to 30 MeV. For a steeply falling energy spectrum, the energy integral will be dominated at the lowest energies (about 1 MeV in the cases here). Here j is the charged particle inten-

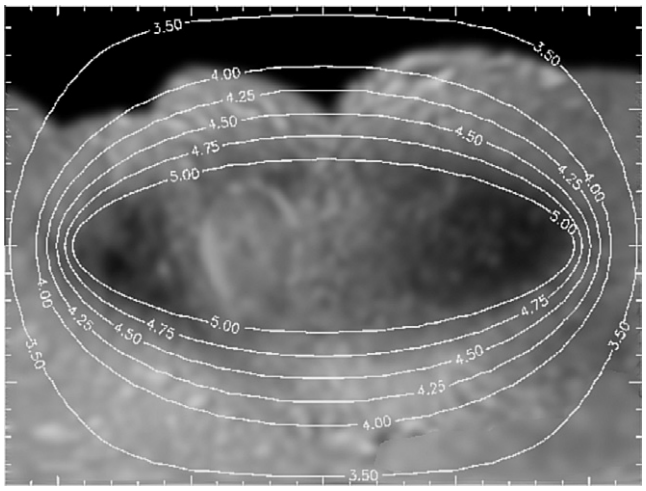

Fig. 17. IR/UV color ratio map of leading hemisphere of Mimas with contours of power into the surface per unit area overlain. Map data are from Fig. 2 but have been smoothed using a low-pass filter to suppress local features and map noise. Contours created in the same manner as described in Paranicas et al. (2010, their Fig. 8), using data from Cassini/MIMI. The contour at $\sim 10^{(4.75)}$ MeV/(cm^2 s) most closely matches the edge of the Mimas equatorial band. The circular bright patch at center left of the lens is the 120-km-wide Herschel crater. Map extends from −90° to 90° latitude and −20°W to 200°W longitude. See text for additional details.

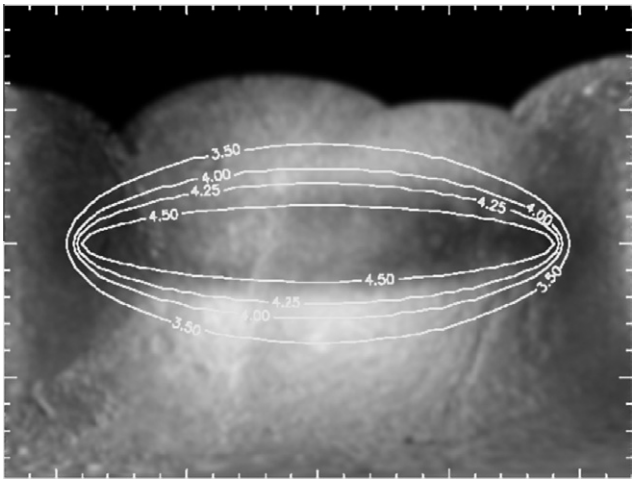

Fig. 18. IR/UV color ratio map of leading hemisphere of Tethys with contours of power into the surface per unit area overlain. Map data are from Fig. 2 but have been smoothed using a low-pass filter to suppress local features and map noise. Some longitudinal structure in the band in evident when smoothed, including an increase in ratio (redness) along the center of the band and along the southern edge (and likely northern edge also). Contours created in the same manner as described in Paranicas et al. (2010, their Fig. 8), using data from Cassini/MIMI. The contour at $10^{(4.25)}$ MeV/(cm^2 s) most closely matches the edge of the Tethys equatorial band. Map extends from −90° to 90° latitude and −20°W to 200°W longitude. See text for additional details.

sity, derived by averaging electron data from Cassini LEMMS (Low Energy Magnetospheric Measurement System; Krimigis et al., 2004) over time periods when the spacecraft was close to the orbital distance of a given moon. Figs. 17 and 18 show contours of log MeV cm^{-2} s^{-1}) on Mimas and Tethys, overlain on leading hemisphere maps of IR/UV ratio intensity from Fig. 2. These gradient contours very closely match the locations and shapes of the observed equatorial bands (or lenses) on both satellites and at similar dose contours (at approximately $10^{4.5}$ MeV cm^{-2} s^{-1}). The physical nature of this transition is not yet clear but suggests that a critical energy flux is required to physically alter the surface.

Because Mimas (radial distance ≈3.08 Saturn radii, R_s) is in a more intense radiation environment than Tethys (≈4.89 R_s), the population of particles above the critical energy from about 1 MeV and up, does not decrease as quickly with increasing energy. In other words, the radiation belt at Mimas is populated with relatively more electrons well above 1 MeV. In comparison, at the location of Tethys, the energy spectrum falls off more rapidly with increasing energy. As noted above, the more energetic electrons reach the highest latitudes on the leading hemisphere. Thus, we estimate the dose into the leading hemisphere of the saturnian satellites from energetic electrons to be greatest and reach the highest latitudes within the most intense parts of the electron radiation belts (within the orbit of Dione). Deep within the belts, that is, at Mimas, the latitudinal spread of electron dose on the leading hemisphere of the satellites will be most pronounced.

So, given the above correlations, how do the >1 MeV electrons affect the surface? These MeV electrons appear to affect the reflectance properties of Tethys and Mimas in a manner opposite to what one often associates with radiation effects. Although such electrons also trigger surface chemistry and, hence, possible absorption features sensible by the Cassini ISS UV filter set, these electrons also penetrate very deeply, forming defects and small voids in the ice that act as scattering centers (Johnson et al., 1985; Johnson and Jesser, 1997). Therefore, we suggest that brightening seen in the UV and, hence, a lowering of the IR/UV ratio are in fact due primarily to *enhanced scattering* in the wavelength regime associated with the UV filter. An important test of this hypothesis would be to image the leading hemispheres of Mimas and Tethys at the shortest UV wavelengths (the UV1 and UV2 filters, which are not used here due to lack of areal coverage). The latter filters are the most sensitive to the 0.26-μm ozone absorption, and surface O_3 abundance is predicted to be elevated within the UV-bright equatorial bands.

An unresolved question here concerns why the equatorial band is IR-dark on Tethys but not on Mimas. Although the inherent brightness of the Mimas band is still darker than on Tethys, this behavior could be related to the inherently higher albedo of Tethys (e.g., Verbiscer et al., 2007) and perhaps subtle compositional differences between the two satellites (i.e., deviations from pure water ice). Additional color imaging would be helpful in explaining this particular property.

4.4. Enceladus

The odd global color patterns and active geology of Enceladus immediately raise the likelihood that processes unique to Enceladus are creating the surface patterns we see. Enceladus space is strongly dominated by the E-ring, which is most dense near Enceladus and is resupplied by plume material from the active south polar region. In a separate paper (Schenk et al., in preparation), we show that this pattern is well matched by the predicted fallout pattern (Kempf et al., 2010) of redeposited plume material, a situation unique to Enceladus. The main point here is that this local deposition, and by association the E-ring particles themselves, which are densest nearest Enceladus, appear to block or mask the formation of the features seen on the other icy satellites. These include the equatorial lenses on neighboring Mimas and Tethys and the reddish asymmetries centered squarely on the leading and trailing hemispheres and the processes forming them.

4.5. A ring at Rhea?

At high resolution (Figs. 13–15), the blue patches along Rhea's equator are associated with older impact features and are not associated with any obvious, endogenic tectonic process, as no linear or other tectonic fabric is apparent. While large basins and tidally disrupted comets can both produce linear secondary crater chains (Schenk et al., 1996), the location of the patches within a degree or two of the equator and the lack of any large basins in line with this feature (Fig. 1) rule out impact by secondary craters, and neither secondaries nor split comets produce chains that exceed 180° in circumference.

A thin/diffuse ring/disk or halo surrounding Rhea and currently confined close to the equator has been reported (Jones et al., 2008b), and Jones et al. (2008a) have proposed a relationship between the unusual equatorial color pattern and the possible debris disk or halo. More specifically, they proposed that these features, which we now know to be a circumferential "blue great circle" on Rhea might be directly related to impact of ring material on its surface. We generally support the conclusion that the equatorial feature is due to the impact of orbiting debris, but it does not necessarily imply that such debris is orbiting currently (i.e., the equatorial feature may have been created in the geological past).

While first "detected" as unusual charged particle absorptions by Cassini's plasma and magnetospheric instruments (Jones et al., 2008b), Rhea's putative debris disk has not been observed in the visible or near-infrared (Pitman et al., 2008; Tiscareno et al., 2010). Further, the nature of the particles within this ring/disk is unknown, and although the initial magnetospheric results suggested that it would be dominated by fragments decimeters in size (Jones et al., 2008b), detailed analysis of ISS images by Tiscareno et al. (2010) could find no particle size distribution that could

simultaneously explain the charged particle data and imaging constraints.

Regardless of the present situation surrounding Rhea, with respect to the equatorial blue features (which we stress are real), collisional diffusion would be expected to broaden a hypothetical source debris disk, and allow some of the disk particles to strike the surface of Rhea, preferentially in the equatorial plane. The impact of circum-satellite ring material on Rhea may thus provide insight into the dynamics and nature of the particles within such ring/disks. The narrowness of the blue great circle feature indicates that any source debris disk remained confined within a degree or two of Rhea's equatorial plane, which is not unexpected if the debris density is great enough and long-lived enough to evolve collisionally. Our surface imaging results might also imply that any such ring/disk contained relatively little micron-sized dust, because such dust might be perturbed out of the equatorial plane by non-gravitational forces, and therefore coat Rhea more broadly. At present we see no evidence of any broad color shoulders adjacent to the main blue great circle.

An additional constraint from imaging of the blue patches in Figs. 13–15 is their preference for local ridge crests and east-facing slopes in particular, which suggests that high-standing topography caught or blocked ring or disk particles as they approached the surface. Although the imaging suggest a preference for east-facing slopes, uncertainty remains as to whether impacting material came predominantly from the east, suggesting the possibility of retrograde orbits.

The high resolution imaging in Figs. 13–15 reveals the clumpy and discontinuous nature of the blue patches. The resolution of the blue patches into discrete splotches and crater rimwall deposits can be explained in two ways. First, craters within the patches could be primary impact features related to impact of solid ring objects. With scaling from McKinnon and Schenk (1995), and assuming highly oblique impacts at a circular orbital speed of $\sim$450 m s^{-1} (we neglect Rhea's equatorial rotational velocity of 12 m s^{-1}), and similar impactor and surface densities, the sizes of the putative craters in Fig. 13 imply maximum impactor or fragments sizes on the order of 100 m to several km. It unlikely that such bodies would have gone unnoticed by *Cassini*, if such a population were still in orbit, especially as more copious (and visible!) small particles would be generated by collisions (Tiscareno et al., 2010).

Rather, the bluish craters in Fig. 14 would more likely have formed during a discrete period of time when large debris fragments were more prevalent, perhaps shortly after ring formation, and are recognized as such only because they clustered together (though there is no obvious physical reason for such clustering). These craters would have to have formed long enough ago that bright rays initially formed (e.g., Figs. 6 and 9) would be erased, but recently enough that bluish rimwalls would be retained. In any case, the clustering could be an artifact of preservation.

Alternatively, if Rhea's ring always consisted of only small fragments a few meters or so in size, any ring material reaching the surface of Rhea would not have been large enough to form craters we can observe. The deposits observed in Fig. 14 would then be preexisting craters along the track of the particles where the rimwall surfaces have been disrupted by relatively smaller-sized ring material, material incapable of forming primary craters resolvable in these images, but able to remobilize the regolith and re-expose the fresh bluish ice commonly seen elsewhere in younger crater rimwalls, and potentially explaining the bluish color of the equatorial feature on Rhea. The blue-colored craters within this patch are not obviously of the same relative age, suggesting that disruption of preexisting surfaces by repeated impacts of small particles may indeed be the more likely explanation. If so, the strong bluish color indicates that formation occurred recently and these may be among the most recently formed features on the surface. On the other hand, the surface features we observe might date from an earlier time, as no bright rays have been observed in association with the equatorial deposits. This would imply that sufficient time has lapsed for ray erasure to have occurred but not sufficient time to erase the blue crater rims associated with relatively young impact craters elsewhere on Rhea. High-resolution color and stereo mapping of other splotches may be required to determine their origin more confidently.

Presumably, ring material about a midsize satellite such as Rhea represents debris launched by one or more impacts on its surface. The very young, 80-km-wide impact crater Inktomi (Figs. 1 and 6) has a very extensive bright ray pattern, and as one of the (if not the youngest) known major impact crater in the Saturn system, it could have easily launched at least a modest amount of debris into orbit (inter-particle collisions and Saturn's gravity ensure that not *all* ejecta return immediately to Rhea [e.g., Alvarellos et al., 2005]). But as noted above, the lack of bright ejecta in association with the blue deposits may indicate that the reimpact of orbiting debris was not recent (or that the ring impacts are very small). They are thus unlikely to be associated with Inktomi. In addition, the asymmetric ejecta pattern at Inktomi indicates impact from the west, not the east as would be required to place some fraction of the ejecta into close retrograde orbit. All told, even though it is tempting to relate the formation of this youthful crater with the equatorial blue patches (if not the electron dropouts seen near Rhea [Jones et al., 2008b]), we must conclude that the equatorial features on Rhea appear to relate to an earlier debris ejection event.

That the equatorial feature follows a great circle, nearly perfectly oriented on Rhea's equator, indicates that whatever the origin of the orbiting debris, there was sufficient amount to collisionally evolve and collapse into Rhea's equatorial plane. The 1.8° inclination is, however, not expected. Although the control solution developed here has been stable despite the addition of new image data sets in 2010, suggesting the 1.8° offset is real, there may still be a minor error in the current control network. The apparent 1.8° inclination of the great circle is barely within the margin of error of the equator for the current coordinate system for Rhea (though we note inconsistent latitudes of this order for features near 180°W in other basemaps[2]). Anticipated image acquisition in the current north polar gap after Saturn equinox in 2009 should reduce these errors to less than a degree and confirm the true orientation of the circle with respect to the equator.

If the inclination of the equatorial feature is real, it could be explained by true polar wander of Rhea's figure. Rhea is a slow rotator (not very oblate), and an uncompensated impact crater in the 100-km-diameter class could cause a reorientation of this magnitude (Nimmo and Matsuyama, 2007). In our particular case (and for our control solution), the reorientation would have to be either along the $\sim$190°W (northern hemisphere) or 20°W (southern hemisphere) meridians. No obvious crater candidates present themselves in these locations, and if the positive rim and ejecta mass around a crater is accounted for (Schroeter's rule), the crater required to drive a $\sim$2° reorientation moves into the basin size class.

The pattern of blue equatorial patches/deposits changes character when it crosses from the leading onto the trailing hemisphere of Rhea (Figs. 6 and 10). The change from a bluish to a dark but apparently uncolored deposit suggests that the alteration of the trailing hemisphere, by the exogenic contaminants that are also responsible for the strong hemispheric IR/UV signature may also alter the color of the blue great circle if it not a currently forming feature. Deposits related to the extensive fracture system on the

[2] Compare Fig. 24.6 in Roatsch et al. (2009), or http://www.photojournal.jpl.nasa.gov/catalog/PIA08343, with http://www.planetarynames.wr.usgs.gov/image/rhea_comp.pdf.

trailing hemisphere (Fig. 1) may also mask the colors of the feature or have otherwise disrupted the surface in specific regions, but not across the entire hemisphere. We note that orbital decay of ring material cannot accumulate on one hemisphere preferentially, as even an eccentric ring or ring arc will precess. The simplest explanation is probably that the greater influence of dark-particle implantation and magenetospheric bombardment on the trailing hemisphere of Rhea have masked or altered this equatorial feature, or altered the surface in such a way as to prevent the formation or exposure of bluish material. Available color coverage is weakest on this hemisphere (ranging from 0.75 to 1.5 km/pixel resolution); additional high-resolution color mapping is required to test these conjectures.

Though lacking topographic expression, the unusual linear and equatorial configuration of Rhea's blue circle is surprisingly similar to that of Iapetus' equatorial ridge (Porco et al., 2005; Giese et al., 2008); they are the only two known features in the Solar System uniquely tied to the equator of a major planetary surface (though among small bodies, the Asteroid 1999 KW_4 A and the saturnian ringmoons Pan and Atlas come to mind). Although the blue patches form on the tops of some preexisting ridges, no evidence of an equatorial ridge is seen in either limb images or a global DEM (digital elevation model) of Rhea (see Figs. 13 and 14). The ~70 km wide and 13 km high Iapetus ridge (Giese et al., 2008) extends in a structurally coherent form from approximately −23°W to 213°W longitude on that satellite, beyond which is breaks up into discontinuous segments or peaks or disappears altogether. This discontinuous section is reminiscent of the discontinuous nature of the blue great circle on Rhea (and its possible missing section near 270–340°W).

The unique Iapetus equatorial ridge has led to several suggestions for its origin, including deposition of a primordial ring onto the surface due to collisional diffusion, possibly augmented by gas drag in a Iapetan proto-atmosphere (Ip, 2006). Despite the prominence of this feature, no similar linear ridges have been found on any other midsize or larger icy satellites. Concluding that the Rhea feature is indeed the signature of the impact of (small amounts) of Rhea ring material supports the general conclusion that circum-satellite ring/disk material can make it to the surface of a body. This in turn supports Ip's (2006) interpretation, as opposed to endogenic mechanisms that have been proposed for the ridge. The fact that no topographic pile (or excavated trough) has formed on Rhea indicates that its ring must have been very low mass compared to that proposed for Iapetus, but this is logical as the Iapetus ridge is an ancient (if not primordial) feature, whereas the Rhea color pattern is relatively geologically young and ring material may be less stable around a satellite orbiting in much closer proximity to Saturn. These and other details remain to be explored, however.

5. Summary

Color mapping of the five inner midsize icy satellites of Saturn reveals that their surfaces record several ongoing dynamical processes that vary with distance from Saturn and from Enceladus (summarized in Figs. 19 and 20). Indeed, although geologic features such as rayed craters, crater rimwalls and tectonic scarps and some geologic units have distinctive color signatures, the fundamental color properties of these bodies are all controlled by these global-scale processes.

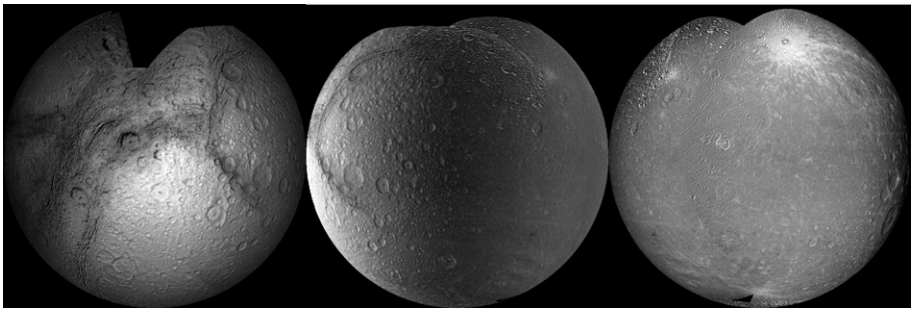

Fig. 19. From left-to-right, orthographic projections of the trailing, anti-saturnian and leading hemispheres of Dione (from Fig. 2) showing the global color asymmetries characteristic of the three icy satellites Tethys, Dione and Rhea. Apparent features include the strong peak in redness at the center of the trailing hemisphere, the broader reddening and the reddish crater ray patterns across the leading hemisphere, and the division between the two hemispheres along the center 180° meridian of the anti-Saturn hemisphere. Not shown (or found on Dione) is the broad equatorial leading-side band seen on Tethys and Mimas.

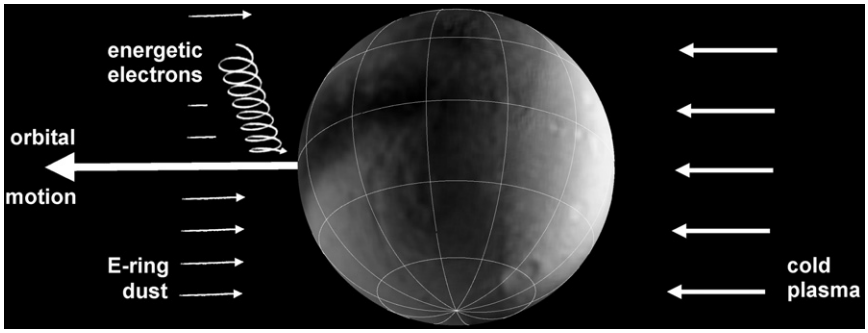

Fig. 20. Cartoon illustrating the basic physical processes proposed to be responsible for global color patterns on the midsize icy satellites of Saturn. Not shown are deposition of particles from circum-satellite debris disks along the equator (as seen at Rhea). View shows sub-saturnian hemisphere, highlighting leading and trailing reddening and blue equatorial band. Cpld plasma may include entrained nanoparticles.

(a-c) The outer three, Tethys, Dione, and Rhea are dominated by two hemispheric color asymmetries in the form of enhanced reddening (higher IR/UV ratios) centered on the leading and trailing hemispheres (Fig. 19). The enhancement is significantly stronger on the trailing hemisphere where it is associated with lower albedo material. The asymmetry on Mimas is seen weakly and only on the trailing hemisphere. These patterns are likely related to two or more competing mechanisms. The trailing hemisphere reddening is likely due to (1) thermal and suprathermal plasma bombardment and (2) implantation of small dark grains with attendant surface chemistry alteration. Simultaneously, (3) E-ring deposition appears to be coating or altering the leading hemispheres of satellites outside Enceladus' orbit and the trailing hemisphere of satellites interior to Enceladus (i.e., Mimas).

(d) On Enceladus the global color asymmetry is offset ~40° to the west compared to the other satellites. The pattern can be shown to match the predicted pattern for redeposition of plume material back onto Enceladus' surface (Kempf et al., 2010; Schenk et al., in preparation). In a sense this can be considered a form of E-ring deposition similar to that seen on the other satellites except that here on Enceladus the fallout pattern is more tightly controlled by near-plume dynamics and a well-outlined surface pattern results.

(e) A fifth process involves the bombardment of very energetic (>1 MeV) electrons onto the leading hemispheres of Mimas and Tethys, forming relatively bluish colored lens-shaped zones along the equatorial zones of both satellites. No similar features are observed on the other satellites, but Dione and Rhea lie further out where the energetic electron density falls off rapidly and Enceladus may be shielded by the densest regions of the E-ring within which it resides.

(f) A sixth process involves the impact of circum-satellite material onto the surface. The only known possible occurrence is the series of blue splotches aligned along the equator of Rhea, interpreted to be the deposition or disturbance of the surface due to the impact of circum-orbital debris in the equatorial plane of Rhea. We note that a similar process has been proposed to explain the equatorial ridge on Iapetus (Ip, 2006), although no discrete build-up of material appears to have occurred on Rhea.

Additional investigation will be required to answer unresolved issues raised by these patterns. First among these is an understanding of the physical processes that occur as these color features form. Little is known about the composition and structure of the surface and how it has been altered by the processes described here. For example, our mapping does not describe the photometric behavior of these deposits. The color features could have different phase functions. Indeed, the equatorial band on Tethys looks significantly different in the very low phase angle color sequences of that hemisphere that are currently available, an aspect we were not able to pursue here. Mapping photometric properties such as the opposition surges and phase functions of each of the color features could reveal differences in the porosity, grain size or other properties of these deposits. Additional high resolution VIMS mapping should also shed light on compositional and grain-size variations across the surfaces. Mapping of geologic features on different hemispheres could also address the issue of determining the relative rates of surface alteration due to these processes.

Note added in proof

Since our initial submission, the Cassini CIRS has discovered a thermal anomaly on Mimas' leading hemisphere geographically coincident with the lens-shaped color anomaly reported here (Howett, C., Spencer, J.R., Pearl, J.C., Hurford, T., Segura, M., Schenk, P., Paranicas, C., 2010, Unexplained surface temperature anomalies on Mimas, AGU Meeting of the Americas, Abs. #P34A-06). If our electron bombardment explanation is correct, we expect a similar thermal anomaly on Tethys.

Acknowledgments

We thank the reviewers, Bob Carlson and Ralf Jaumann. WBM thanks NASA Cassini Data Analysis Program Grants NNX07AE80G and NNX07AJ79G for support of this research.

References

Alvarellos, J.L., Zahnle, K.J., Dobrovolskis, A.R., Hamill, P., 2005. Fates of satellite ejecta in the Saturn system. Icarus 178, 104–123.
Brown, R.H. et al., 2006. Composition and physical properties of Enceladus' surface. Science 311, 1425–1428.
Buratti, B.J., Mosher, J.A., Johnson, T.V., 1990. Albedo and color maps of the saturnian satellites. Icarus 87, 339–357.
Buratti, B.J., Mosher, J.A., Nicholson, P.D., McGee, C.A., French, R.G., 1998. Near-infrared photometry of the saturnian satellites during ring plane crossing. Icarus 136, 223–231.
Carbary, J.F., Mitchell, D.G., Krupp, N., Krimigis, S.M., 2009. L shell distribution of energetic electrons at Saturn. Geophys. Res. Lett. 114. doi:10.1029/2009JA014341.
Carlson, R.W. et al., 1999. Hydrogen peroxide on the surface of Europa. Science 283, 2062–2064.
Carlson, R.W., Calvin, W.M., Dalton, J.B., Hansen, G.B., Hudson, R.L., Johnson, R.E., McCord, T.B., Moore, M.H., 2009. Europa's surface composition. In: Pappalardo, R.T., McKinnon, W.B., Khurana, K.K. (Eds.), Europa. Univ. of Arizona Press, Tucson, pp. 283–327.
Chapman, C.R., McKinnon, W.B., 1986. Cratering of planetary satellites. In: Burns, J.A., Matthews, M.S. (Eds.), Satellites. Univ. of Arizona Press, Tucson, pp. 492–580.
Clark, R.N. et al., 2008. Compositional mapping of Saturn's satellite Dione with Cassini VIMS and implications of dark material in the Saturn system. Icarus 193, 372–386.
Dikarev, V.V., 1999. Dynamics of particles in Saturn's E ring: Effects of charge variations and the plasma drag force. Astron. Astrophys. 346, 1011–1019.
Dones, L., Chapman, C.R., McKinnon, W.B., Melosh, H.J., Kirchoff, M.R., Neukum, G., Zahnle, K.J., 2009. Icy satellites of Saturn: Impact cratering and age determination. In: Dougherty, M.K., Esposito, L.W., Krimigis, S.M. (Eds.), Saturn from Cassini–Huygens. Springer, Dordrecht, pp. 613–635.
Elder, C., Helfenstein, P., Thomas, P., Veverka, J., Burns, J.A., Denk, T., Porco, C., 2007. Tethys' mysterious equatorial band. Bull. Am. Astron. Soc. 39, 429.
Giese, B., Denk, T., Neukum, G., Roatsch, T., Helfenstein, P., Thomas, P.C., Turtle, E.P., McEwen, A., Porco, C.C., 2008. The topography of Iapetus' leading side. Icarus 193, 359–371.
Grundy, W.M. et al., 2007. New Horizons composition mapping, topography, and photometry of Europa and Ganymede. Science 318, 234–237.
Hamilton, D.P., 1993. Motion of dust in a planetary magnetosphere: Orbit-averaged equations for oblateness, electromagnetic, and radiation forces with application to Saturn's E ring. Icarus 101, 244–264 (Erratum: Icarus 103, 161).
Hamilton, D.P., Burns, J.A., 1994. The origin of Saturn's E ring: Self-sustained, naturally. Science 264, 550–553.
Hendrix, A.R., Johnson, R., 2009. Europa: A new look at Galileo UVS data. Lunar Planet. Sci. Abstract 2526. XL, Houston TX (CD-ROM).
Horanyi, M., Burns, J.A., Hamilton, D.P., 1992. The dynamics of Saturn's E-ring particles. Icarus 97, 248–259.
Ip, W., 2006. On a ring origin of the equatorial ridge of Iapetus. Geophys. Res. Lett. 33, L16203.
Jaumann, R. et al., 2008. Distribution of icy particles across Enceladus' surface as derived from Cassini–VIMS measurements. Icarus 193, 407–419.
Jaumann, R., Clark, R.N., Nimmo, F., Hendrix, A.R., Buratti, B.J., Denk, T., Moore, J.M., Schenk, P.M., Ostro, S.J., Srama, R., 2009. Icy satellites: Geological evolution and surface processes. In: Dougherty, M.K., Esposito, L.W., Krimigis, S.M. (Eds.), Saturn from Cassini–Huygens. Springer, Dordrecht, pp. 637–682.
Johnson, R.E., Jesser, W.A., 1997. O_2/O_3 micro-atmospheres in the surface of Ganymede. Astrophys. J. 480, L79–L82.
Johnson, R.E., Barton, L.A., Boring, J.W., Jesser, W.A., Brown, W.L., Lanzerotti, L.J., 1985. Charged particle modification of ices in the saturnian and jovian systems. In: Klinger, J. (Ed.), Ices in the Solar System. D. Reidel, Dordrecht, pp. 301–315.
Johnson, R.E., Carlson, R.W., Cooper, J.F., Paranicas, C., Moore, M.H., Wong, M.C., 2004. Radiation effects on the surfaces of the Galilean satellites. In: Bagenal, F., Dowling, T., McKinnon, W. (Eds.), Jupiter – The Planet, Satellites and Magnetosphere. Cambridge University Press, Cambridge, UK, pp. 485–512.
Johnson, R.E., Fama, M., Liu, M., Baragiola, R.A., Sittler, E.C., Smith, H.T., 2008. Sputtering of ice grains and icy satellites in Saturn's inner magnetosphere. Planet. Space Sci. 56, 1238–1243.

Jones, G., et al., 2008a. A debris disk surrounding Saturn's moon Rhea. Eos Trans. AGU. Abstract #P32A-04.
Jones, G.H. et al., 2008b. The dust halo of Saturn's largest icy moon, Rhea. Science 319, 1380–1383.
Kempf, S. et al., 2005. Composition of saturnian stream particles. Science 307, 1274–1276.
Kempf, S., and the CDA Science Team, 2006. Structure and sources of Saturn's E-ring, Bull. Am. Astron. Soc. 38, 572. Abstract #47.03.
Kempf, S., Beckmann, U., Schmidt, S., 2010. How the Enceladus dust plume feeds Saturn's E ring. Icarus 206, 446–457. doi:10.1016/j.icarus.2009.09.016.
Khurana, K.K., Pappalardo, R.T., Murphy, N., Denk, T., 2007. The origin of Ganymede's polar caps. Icarus 191, 193–202.
Krimigis, S.M. et al., 2004. Magnetospheric imaging instrument on the Cassini mission to Saturn/Titan. Space Sci. Rev. 114, 233–329.
Krupp, N. et al., 2009. Energetic particles in Saturn's magnetosphere during the Cassini nominal mission (July 2004–July 2008). Planet. Space Sci. 57, 1754–1768. doi:10.1016/j.pss.2009.06.010.
Mauk, B.H., Mitchell, D., McEntire, R., Paranicas, C., Roelef, E., Williamns, D., Krimigis, S., 2004. Energetic ion characterizations and neutral gas interactions in Jupiter's magnetosphere. J. Geophys. Res. 109, A09S12.
McEwen, A., 1991. Photometric functions for photoclinometry and other applications. Icarus 92, 298–311.
McKinnon, W.B., Schenk, P.M., 1995. Estimates of comet fragment masses from impact crater chains on Callisto and Ganymede. Geophys. Res. Lett. 22, 1829–1832.
Moore, J.M., 1984. The tectonic and volcanic history of Dione. Icarus 59, 205–220.
Moore, J., Schenk, P., 2007. Topography of endogenic features on saturnian mid-sized satellites. Lunar Planet. Sci. XVIII. Abstract 2136. Lunar and Planetary Institute, Houston, TX.
Nimmo, F., Matsuyama, I., 2007. Reorientation of icy satellites by impact basins. Geophys. Res. Lett. 34, L19203.
Noll, K.S., Rousch, T.L., Cruikshank, D.P., Johnson, R.E., Pendleton, Y.J., 1997. Detection of ozone on Saturn's satellites Rhea and Dione. Nature 388, 45–47.
Pang, K.D., Voge, C.C., Rhoads, J.W., Ajello, J.M., 1984. The E ring of Saturn and satellite Enceladus. J. Geophys. Res. 89, 9459–9470.
Paranicas, C., Carlson, R.W., Johnson, R.E., 2001. Electron bombardment of Europa. Geophys. Res. Lett. 28, 673–676.
Paranicas, C. et al., 2008. Sources and losses of energetic protons in Saturn's magnetosphere. Icarus 197, 519–525.
Paranicas, C., Cooper, J.F., Garrett, H.B., Johnson, R.E., Sturner, S.J., 2009. Europa's radiation environment and its effects on the surface. In: Pappalardo, R.T., McKinnon, W.B., Khurana, K.K. (Eds.), Europa. Univ. of Arizona Press, Tucson, pp. 529–544.
Paranicas, C., et al., 2010a. Asymmetries in Saturn's radiation belts. J. Geophys. Res. 115, A07216. doi:10.1029/2009JA014971.
Paranicas, C., et al., 2010b. Transport of energetic electrons into Saturn's inner magnetosphere. J. Geophys. Res. doi:10.1029/2010JA015853.
Pitman, K., Buratti, B., Mosher, J., Bauer, J., Momary, T., Brown, R., Nicholson, P., Hedman, M., 2008. First high solar phase angle observations of Rhea using Cassini VIMS: Upper limits on water vapor and geologic activity. Astrophys. J. 680, L65–L68.
Plescia, J.B., 1983. The geology of Dione. Icarus 56, 255–277.
Porco, C.C. et al., 2004. Cassini imaging science: Instrument characteristics and anticipated scientific investigations at Saturn. Space Sci. Rev. 115, 363–497.
Porco, C.C. et al., 2005. Cassini imaging science: Initial results on Phoebe and Iapetus. Science 307, 1237–1242.
Porco, C.C. et al., 2006. Cassini observes the active south pole of Enceladus. Science 311, 1393–1401.
Roatsch, Th., Jaumann, R., Stephan, K., Thomas, P.C., 2009. Cartographic mapping of the icy satellites using ISS and VIMS data. In: Dougherty, M.K., Esposito, L.W., Krimigis, S.M. (Eds.), Saturn from Cassini–Huygens. Springer, Dordrecht, pp. 763–781.
Roussos, E. et al., 2007. Electron microdiffusion in the saturnian radiation belts: Cassini MIMI/LEMMS observations of energetic electron absorption by the icy moons. J. Geophys. Res. 112, A06214. doi:10.1029/2006JA012027.
Schenk, P., 2010. Atlas of the Galilean Satellites. Cambridge Univ. Press, Cambridge.
Schenk, P., McKinnon, W., 1989. Dark ray and dark floor craters on Ganymede and the provenances of large impactors in the Jovian system. Icarus 89, 318–346.
Schenk, P., Moore, J., 2007. Topography of endogenic features on saturnian mid-sized satellites. Lunar Planet. Sci. XVIII. Abstract 2136. Lunar and Planetary Institute, Houston, TX.
Schenk, P.M., Asphaug, E., McKinnon, W.B., Melosh, H.J., Weissman, P., 1996. Cometary nuclei and tidal disruption: The geologic record of crater chains on Callisto and Ganymede. Icarus 121, 249–274.
Showalter, M.R., Cuzzi, J.N., Larson, S.M., 1991. Structure and particle properties of Saturn's E ring. Icarus 94, 451–473.
Smith, B. et al., 1981. Encounter with Saturn: Voyager 1 imaging science results. Science 212, 163–191.
Stephan, K., et al., 2009. VIMS coverage of Saturn's icy satellite Rhea. Lunar Planet. Sci. Abstract 1377. Lunar and Planetary Institute, Houston, TX.
Stephan, K. et al., 2010. Dione's spectral and geologic properties. Icarus 206, 631–652. doi:10.1016/j.icarus.2009.07.036.
Stooke, P.J., 1989. Tethys: Volcanic and structural history. Lunar Planet. Sci. XX, 1071–1072.
Stooke, P.J., 2002. Tethys and Dione: New geological interpretations. Lunar Planet Sci. XXXIII. Abstract 1553.
Thomas, P.C., 2010. Sizes, shapes, and derived properties of the saturnian satellites after the Cassini nominal mission. Icarus 208, 395–401.
Thomas, P.C. et al., 2007. Shapes of the saturnian icy satellites and their significance. Icarus 190, 573–584.
Tiscareno, M.S., Burns, J.A., Cuzzi, J.N., Hedman, M.M., 2010. Cassini imaging search rules out rings around Rhea. Geophys. Res. Lett. 37, L14205. doi:10.1029/2010GL043663.
Verbiscer, A.J., Veverka, J., 1989. Albedo dichotomy of Rhea: Hapke analysis of Voyager photometry. Icarus 82, 336–353.
Verbiscer, A.J., Veverka, J., 1992. Mimas: Photometric roughness and albedo map. Icarus 99, 63–69.
Verbiscer, A.J., Veverka, J., 1994. A photometric study of Enceladus. Icarus 110, 155–164.
Verbiscer, A., French, R., Showalter, M., Helfenstein, P., 2007. Enceladus: Cosmic graffiti artist caught in the act. Science 315, 815.
Verbiscer, A.J., Skrutskie, M.F., Hamilton, D.P., 2009. Saturn's largest ring. Nature 461, 1098–1100.
Wagner, R., Neukum, G., Giese, B., Roatsch, T., Denk, T., 2007. Geology and geomorphology of Rhea: A first look at the high-resolution Cassini ISS images from the targeted flyby on August 30, 2007. Eos 87. Abstract #P12B-06.
Waite, J.H. et al., 2009. Liquid water on Enceladus from observations of ammonia and ^{40}Ar in the plume. Nature 460, 487–490.